

Predicting room-temperature conductivity of Na-ion super ionic conductors with the minimal number of easily-accessible descriptors

Seong-Hoon Jang,^{1,2} Randy Jalem,² and Yoshitaka Tateyama^{2,3}*

¹ Institute for Materials Research, Tohoku University, 2-1-1 Katahira, Aoba-ku, Sendai, 980-8577, Japan

² Research Center for Energy and Environmental Materials (GREEN), National Institute for Materials Science (NIMS), 1-1 Namiki, Tsukuba, Ibaraki 305-0044, Japan

³ Laboratory for Chemistry and Life Science, Tokyo Institute of Technology, 4259 Nagatsuta, Midori-ku, Yokohama, 226-8501, Japan

*Corresponding author: jang.seonghoon.b4@tohoku.ac.jp

KEYWORDS. materials design, solid electrolytes, beta regression modelling, materials informatics

ABSTRACT. Given the vast compositional possibilities $\text{Na}_nM_mM'_m\text{Si}_{3-p-a}\text{P}_p\text{As}_a\text{O}_{12}$, Na-ion superionic conductors (NASICON) are attractive but complicate for designing materials with enhanced room-temperature Na-ion conductivity $\sigma_{\text{Na},300\text{K}}$. We propose an explicit regression model for $\sigma_{\text{Na},300\text{K}}$ with easily-accessible descriptors, by exploiting density functional theory

molecular dynamics (DFT-MD). Initially, we demonstrate that two primary descriptors, the bottleneck width along Na-ion diffusion paths d_1 and the average Na-Na distance $\langle d_{\text{Na}-\text{Na}} \rangle$, modulate room-temperature Na-ion self-diffusion coefficient $D_{\text{Na},300\text{K}}$. Then, we introduce two secondary easily-accessible descriptors: Na-ion content n , which influences d_1 , $\langle d_{\text{Na}-\text{Na}} \rangle$, and Na-ion density ρ_{Na} ; and the average ionic radius $\langle r_M \rangle$ of metal ions, which impacts d_1 and $\langle d_{\text{Na}-\text{Na}} \rangle$. These secondary descriptors enable the development of a regression model for $\sigma_{\text{Na},300\text{K}}$ with n and $\langle r_M \rangle$ only. Subsequently, this model identifies a promising yet unexplored stable composition, $\text{Na}_{2.75}\text{Zr}_{1.75}\text{Nb}_{0.25}\text{Si}_2\text{PO}_{12}$, which, upon DFT-MD calculations, indeed exhibits $\sigma_{\text{Na},300\text{K}} > 10^{-3} \text{ S}\cdot\text{cm}^{-1}$. Furthermore, the adjusted version effectively fits 140 experimental values with $R^2 = 0.718$.

Inorganic solid electrolytes hold significant promise in advancing solid-state battery technology due to their possible superior electrochemical and thermal stability, as well as decreased flammability when compared to liquid electrolytes, if ideal.¹⁻⁵ Several classes of inorganic solid electrolytes have shown great potential, including Li-ion oxides [such as lithium superionic conductor (LISICON) $\text{Li}_{14}\text{ZnGe}_4\text{O}_{16}$ ⁶ and LLZO $\text{Li}_7\text{La}_3\text{Zr}_2\text{O}_{12}$]⁷ Li-ion sulfides (LGPS $\text{Li}_{10}\text{GeP}_2\text{S}_{12}$),⁸ and Na-ion sulfides ($\text{Na}_nM_mM'_mS_4$; M and M' are metal ions).^{9,10} Among these, Na-ion oxides known as Na-ion superionic conductors (NASICON) has attracted considerable attention due to the earth-abundant sodium, structural and thermal stability, and notably high ion conductivity facilitated by its unique three-dimensional “skeleton” structure.¹¹⁻¹³

NASICON, represented by the generalized chemical formula $\text{Na}_nM_mM'_m\text{Si}_{3-p-a}\text{P}_p\text{As}_a\text{O}_{12}$, offers the ability to incorporate a wide range of metal ions (M or M') with varying valences and ionic radii, making it a compelling system for designing materials with enhanced Na-ionic conduction.¹⁴ Numerous substitutions have been explored, including divalent ions such as Mg,¹⁵⁻¹⁹ Ca,^{19, 20} Fe,²¹ Co,¹⁷ Zn,^{15, 18} Sr,¹⁹ Cd,¹⁸ and Ba;¹⁹ trivalent ions such as Al,^{18, 22-25} Sc,^{23, 24, 26-30} Cr,^{18, 23, 24, 26, 31-33} Fe,^{18, 21, 23, 24, 26, 32, 33} Ga,^{23, 24} Y,^{23, 24, 34-37} In,^{18, 23, 24, 31, 35, 38} Nd,³⁹ Gd,^{35, 40, 41} Tb,³⁵ Dy,^{35, 42} Er,^{35, 42} and Yb;^{18, 23, 24, 31, 35, 41-43} tetravalent ions such as Ti,^{15, 25, 44-46} Ge,^{25, 44, 45} Zr,^{25, 45} Sn,^{15, 25, 45, 47} Hf,^{25, 44, 45, 48} Ce,^{41, 44} and Th;⁴⁴ and pentavalent ions such as V,¹⁵ Nb,^{15, 28, 49-53} Mo,⁵⁰ and Ta.¹⁵

Given the extensive array of compositions within the framework of $\text{Na}_nM_mM'_m\text{Si}_{3-p-a}\text{P}_p\text{As}_a\text{O}_{12}$, we endeavor to construct an “explicit” regression model for the prediction of room-temperature Na-ion conductivity $\sigma_{\text{Na},300\text{K}}$, utilizing two descriptors easily accessible from the chemical formula only, which is an unexplored avenue in the current literature.

Undertaking exhaustive experimental investigations for all conceivable compositions poses a formidable challenge; hence, we advocate for a theoretical approach, specifically employing density functional theory molecular dynamics (DFT-MD) in conjunction with regression modeling techniques. Herein, we extensively employ the beta regression modeling technique, which offers a flexible framework for analyzing data spanning a wide range of magnitudes in $\sigma_{\text{Na},300\text{K}}$. This technique has hitherto remained unexplored in the realm of energy materials design and presents a timely and pragmatic opportunity to identify NASICON-type solid electrolytes demonstrating excellent $\sigma_{\text{Na},300\text{K}}$ performance, as finding easily-accessible but effective descriptors. Significantly, our model facilitates a comprehensive understanding within the expansive landscape of NASICON-type compositions, providing valuable insights into the specific conditions under which the desired $\sigma_{\text{Na},300\text{K}}$ would be achieved.

Sampling protocol. In this study, we constructed the sampling protocol to build an explicit regression model of $\sigma_{\text{Na},300\text{K}}$ for NASICON-type solid electrolytes, as represented in Fig. 1. We initially collected 19 samples as diverse as possible that represent various types of $\text{Na}_nM_mM'_m\text{Si}_{3-p-a}\text{P}_p\text{As}_a\text{O}_{12}$ for the training dataset of the regression modelling: quaternary, quinary, and senary, and $v(M') = 2, 3$, and 4 ; $v(M')$ is the valence of metal ions M' . The protocol comprises four parts: structure search, data training, model test, and model revision for experimental values.

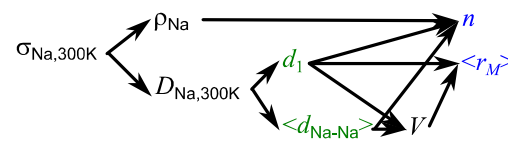
Traning dataset

- Type I: quaternary
- Type II: quinary and $M = \text{Zr}$
- Type III: senary, $M = \text{Zr}$, and $v(M') = 2$
- Type IV: quinary, $M = \text{Zr}$, and $v(M') = 3$
- Type V: senary, $M = \text{Zr}$, and $v(M') = 3$
- Type VI: senary, $M = \text{Zr}$, and $v(M') = 4$

Structure search

- Ewald summation sampling
- ↓
- Geometry-optimization with DFT

Data training

- Single- T "long-time" diagnoses
- ↓ $\Delta\tau = 1 \text{ fs}$, $\tau = 1 \text{ ns}$, and $T = 300 \text{ K}$
- Multivariate beta regression modelling for $D_{\text{Na},300\text{K}}$
- ↓ Found descriptors: d_1 and $\langle d_{\text{Na-Na}} \rangle$
- Demensionality reduction for $\sigma_{\text{Na},300\text{K}}$
- ↓ 
- Identify competitive NASICON with n and $\langle r_M \rangle$
- $\text{Na}_{2.75}\text{Zr}_{1.75}\text{Nb}_{0.25}\text{Si}_2\text{PO}_{12}$: $\sigma_{\text{Na},300\text{K},\text{sim}} > 10^{-3} \text{ S}\cdot\text{cm}^{-1}$

Model test

- Multi- T DFT-MD calculations
- $\Delta\tau = 1 \text{ fs}$, $\tau = 600 \text{ ps}$,
- and $T = 300, 500, 700, \text{ and } 900 \text{ K}$
- $\text{Na}_{2.75}\text{Zr}_{1.75}\text{Nb}_{0.25}\text{Si}_2\text{PO}_{12}$: $\sigma_{\text{Na},300\text{K}} > 10^{-3} \text{ S}\cdot\text{cm}^{-1}$

Model revision for experimental values

- Introduce probit function
- $R^2 = 0.718$ for $n_{\text{data}} = 140$

Fig. 1 Sampling protocol to build an explicit regression model of $\sigma_{\text{Na},300\text{K}}$ for NASICON-type solid electrolytes. Given the representative samples for various types of NASCION compositions $\text{Na}_nM_mM'_m\text{Si}_{3-p-a}\text{P}_p\text{As}_a\text{O}_{12}$, the protocol comprises four parts: structure search, data training, model test, and model revision for experimental values. For the denotations, the main text is referred to.

For the structure search, we utilized Ewald summation sampling⁵⁴ and density functional theory (DFT) to optimize the crystal structures of the 19 representative in-silico samples for $\text{Na}_nM_mM'_{m'}\text{Si}_{3-p-a}\text{P}_p\text{As}_a\text{O}_{12}$, starting from the monoclinic structure $\text{Na}_3\text{Zr}_2\text{Si}_2\text{PO}_{12}$ with $C2/c$ symmetry that was determined experimentally.¹¹ Subsequently, we performed DFT-MD calculations for these 19 training samples at room temperature ($T = 300$ K), which we call single- T “long-time” diagnoses (with a time step of $\Delta\tau = 1$ fs over a simulation time of $\tau = 1$ ns).¹⁰ Based on the obtained data, we exhaustively explored multivariate beta regression models,⁵⁵⁻⁵⁷ incorporating 17 features encompassing electrostatic, diffusion-pathway, and geometrical characteristics. Here, the adoption of beta regression modelling was employed to effectively distinguish between low- and high-performance samples in a manner similar to binary classification. The selection of the optimal model was based on the highest value of the pseudo-goodness-of-fit metric R^2_{pseudo} .⁵⁶ Herein, we found two primary descriptors; the bottleneck width along the diffusion paths for Na-ions d_1 and the average Na-Na distance $\langle d_{\text{Na}-\text{Na}} \rangle$ play pivotal roles in modulating the room-temperature Na-ion self-diffusion coefficients $D_{\text{Na},300\text{K}}$. Then, we introduced two secondary descriptors easily accessible from the chemical formula only; the Na-ion content n as of $\text{Na}_nM_mM'_{m'}\text{Si}_{3-p-a}\text{P}_p\text{As}_a\text{O}_{12}$ affect d_1 , $\langle d_{\text{Na}-\text{Na}} \rangle$, and Na-ion density ρ_{Na} , and the average $\langle r_M \rangle$ of ionic radii r_M for metal ions M and M' (excluding Na-ions)⁵⁸ affect d_1 and $\langle d_{\text{Na}-\text{Na}} \rangle$. Based on the beta regression model above, the easily-accessible descriptors n , n^2 , and $\langle r_M \rangle$ allow for the final explicit form of regression model.

To elucidate the viability of this regression model, we selected the composition $\text{Na}_{2.75}\text{Zr}_{1.75}\text{Nb}_{0.25}\text{Si}_2\text{PO}_{12}$, hitherto unexplored, which was identified as a potential candidate for $\sigma_{\text{Na},300\text{K},\text{sim}} > 10^{-3} \text{ S}\cdot\text{cm}^{-1}$ ($\sigma_{\text{Na},300\text{K},\text{sim}}$ is the simulated value of $\sigma_{\text{Na},300\text{K}}$ by using the regression

model). It exhibited thermodynamic phase stability, that is, low decomposition energy above the convex hull ($E_{\text{hull}} = 6.49 \text{ meV}\cdot\text{atom}^{-1}$). To estimate not only $\sigma_{\text{Na},300\text{K}}$ but also the Na-ion bulk activation energy E_a , we performed additional DFT-MD calculations for the test sample at multiple temperatures ($T = 300, 500, 700, \text{ and } 900 \text{ K}$), which we call multi- T DFT-MD calculations (with $\Delta\tau = 1 \text{ fs}$ and $\tau = 600 \text{ ps}$).¹⁰ The results confirmed the validity of the model: $\sigma_{\text{Na},300\text{K}} = 1.45 \times 10^{-3} \text{ S}\cdot\text{cm}^{-1}$ and $E_a = 232 \text{ meV}$. Then, we extended the regression modelling for the experimental values of $\sigma_{\text{Na},300\text{K}}$. The adjusted model, wherein the probit function of the aforementioned model was introduced, demonstrated the capability to fit 140 experimental values with the goodness-of-fit metric $R^2 = 0.718$.

Building a regression model. Table 1 presents the values of E_{hull} , $\sigma_{\text{Na},300\text{K}}$, the room-temperature Na-ion self-diffusion coefficients $D_{\text{Na},300\text{K}}$, and the R -squared values R^2_{MSD} for the mean squared displacement (MSD) curves regressed against sampled time intervals $\Delta\tau_{\text{MSD}}$ through the single- T “long-time” diagnoses, given the fixed unit cells optimized by using DFT. E_{hull} across the 19 samples showed the structural (meta)stability ($E_{\text{hull}} < 40 \text{ meV}\cdot\text{atom}^{-1}$). Among the total dataset of $n_{\text{data}} = 19$, five samples were classified as low-performance, characterized by $\sigma_{\text{Na},300\text{K}} < 10^{-4} \text{ S}\cdot\text{cm}^{-1}$ and $D_{\text{Na},300\text{K}} < 10^{-9} \text{ cm}^2\cdot\text{s}^{-1}$. These low-performance samples were predominantly observed in the quaternary types. The remaining eight samples were categorized as high-performance, exhibiting $\sigma_{\text{Na},300\text{K}} > 10^{-4} \text{ S}\cdot\text{cm}^{-1}$ and $D_{\text{Na},300\text{K}} > 10^{-9} \text{ cm}^2\cdot\text{s}^{-1}$. In Supplementary Fig. 1, we represent the MSD curves for the 19 samples. Meanwhile, the pristine composition $\text{Na}_3\text{Zr}_2\text{Si}_2\text{PO}_{12}$ exhibited $\sigma_{\text{Na},300\text{K}} = 1.09 \times 10^{-3} \text{ S}\cdot\text{cm}^{-1}$, which aligns with the experimental measurement of the bulk ion conductivity $\sigma_{\text{Na},300\text{K}} \cong 10^{-3} \text{ S}\cdot\text{cm}^{-1}$ as justifying the quality of the data training method.⁵⁹

Table 1 Values for energies E_{hull} above the convex hull, room-temperature Na-ion conductivities $\sigma_{\text{Na},300\text{K}}$, room-temperature Na-ion self-diffusion coefficients $D_{\text{Na},300\text{K}}$, and R -squared values R_{MSD}^2 for the MSD curves regressed against sampled time intervals $\Delta\tau_{\text{MSD}}$, which were estimated by the single- T “long-time” diagnoses (with $\Delta\tau = 1$ fs and $\tau = 1$ ns at $T = 300$ K) for the 19 samples.

Compounds	E_{hull} (meV·atom $^{-1}$)	$\sigma_{\text{Na},300\text{K}}$ (S·cm $^{-1}$)	$D_{\text{Na},300\text{K}}$ (cm 2 ·s $^{-1}$)	R_{MSD}^2
NaTi ₂ P ₃ O ₁₂	20.4	5.47×10^{-7}	2.10×10^{-11}	0.0500
NaGe ₂ P ₃ O ₁₂	16.5	5.55×10^{-7}	1.94×10^{-11}	0.0464
NaZr ₂ P ₃ O ₁₂	0	3.18×10^{-6}	1.36×10^{-10}	0.308
NaZr ₂ As ₃ O ₁₂	0	1.65×10^{-6}	7.85×10^{-11}	0.219
Na ₃ In ₂ P ₃ O ₁₂	37.0	5.88×10^{-3}	8.48×10^{-8}	0.859
Na ₃ Zr ₂ Si ₂ PO ₁₂	0	1.09×10^{-3}	1.62×10^{-8}	0.920
Na _{3.25} Zr _{1.875} Mg _{0.125} Si ₂ PO ₁₂	0.578	5.99×10^{-4}	8.17×10^{-9}	0.881
Na _{3.75} Zr _{1.625} Mg _{0.375} Si ₂ PO ₁₂	5.42	6.15×10^{-5}	7.26×10^{-10}	0.347
Na _{3.25} Zr _{1.875} Ca _{0.125} Si ₂ PO ₁₂	1.76	1.10×10^{-4}	1.51×10^{-9}	0.143
Na _{3.5} Zr _{1.75} Ca _{0.25} Si ₂ PO ₁₂	4.14	1.07×10^{-4}	1.37×10^{-9}	0.0549
Na _{3.75} Zr _{1.625} Zn _{0.375} Si ₂ PO ₁₂	17.1	1.23×10^{-3}	1.46×10^{-8}	0.767
Na _{1.5} Zr _{1.5} Al _{0.5} P ₃ O ₁₂	9.32	1.48×10^{-3}	4.06×10^{-8}	0.942
Na _{1.5} Zr _{1.5} Sc _{0.5} P ₃ O ₁₂	6.46	1.74×10^{-3}	4.97×10^{-8}	0.977
Na _{1.5} Zr _{1.5} Ga _{0.5} P ₃ O ₁₂	16.1	9.03×10^{-4}	2.52×10^{-8}	0.912
Na _{2.875} Zr _{0.125} In _{1.875} P ₃ O ₁₂	36.1	1.71×10^{-3}	2.57×10^{-8}	0.943
Na _{3.375} Zr _{1.625} Sc _{0.375} Si ₂ PO ₁₂	33.6	1.53×10^{-3}	2.01×10^{-8}	0.661
Na ₃ Zr _{1.25} Ti _{0.75} Si ₂ PO ₁₂	17.6	2.08×10^{-3}	2.98×10^{-8}	0.642
Na ₃ Zr _{1.75} Ti _{0.25} Si ₂ PO ₁₂	7.13	1.51×10^{-3}	2.21×10^{-8}	0.928
Na ₃ Zr _{1.75} Sn _{0.25} Si ₂ PO ₁₂	8.13	3.95×10^{-3}	5.81×10^{-8}	0.989

While some of the high-performance samples displayed reliable MSD curves with high R_{MSD}^2 values, the others yielded low R_{MSD}^2 values due to the insufficient occurrence of site-to-site jump events given the low temperature $T = 300$ K. In Supplementary Fig. 1, we additionally illustrate the finite quantities of trajectory samples exhibiting squared displacements surpassing the squared average Na-Na distances $\langle d_{\text{Na-Na}} \rangle^2$, which are related to the sizes of $D_{\text{Na},300\text{K}}$ [see Supplementary Fig. 2]. Consequently, the MSD curves suffered from considerable noise, leading to lower reliability of the $D_{\text{Na},300\text{K}}$ and $\sigma_{\text{Na},300\text{K}}$ values. To address the uncertainties associated with $D_{\text{Na},300\text{K}}$, multivariate beta regression modelling was employed to clearly differentiate between low- and high-performance samples as well as to elucidate the descriptors with significant contribution towards $D_{\text{Na},300\text{K}}$ prediction. The beta regression response function based on Eq. (12) (described in the Method section) was given by

$$\eta = 0.261 \log_{10} D_{\text{Na},300\text{K}} + 2.82. \quad (1)$$

In the present regression modelling, a total of 17 features (descriptor candidates) were included, comprising two electrostatic, eight diffusion-pathway, and seven geometrical features (see Supplementary Note 1 for details and Supplementary Table 2 for the feature dataset). Among the various fitted models, the one whose sigmoid function response $\bar{\eta}$ fits η [see Eqs. (10)–(12) in the Method section] with the highest R_{pseudo}^2 (see Supplementary Note 2) is composed of two z-scored primary descriptors as follows:

$$h = 1.28 z[d_1] - 1.26 z[\langle d_{\text{Na-Na}} \rangle] + 0.719, \quad (2)$$

with the common precision $\varphi = 7.49$ (see Supplementary Note 2): $R_{\text{pseudo}}^2 = 0.797$ (see Fig. 2). The Pearson correlation coefficient between d_1 and $\langle d_{\text{Na-Na}} \rangle$ was given as $r(d_1, \langle d_{\text{Na-Na}} \rangle) =$

.204 (see Supplementary Note 2), indicating the absence of the significant multicollinearity issue within Eq. (2). To further evaluate whether these two descriptors are indeed predictive, we repeatedly compute R_{pseudo}^2 but with the omission of 4 random samples ($n_{\text{data}} = 15$; n_{data} is the number of data) for 100 times. The mean and the standard deviation for the R_{pseudo}^2 values were given as 0.803 and 0.0368, respectively, indicating its robustness. Then, from Eqs. (2), (10), and (11), we defined $\sigma_{\text{Na},300\text{K,sim}}$ as a function of d_1 and $\langle d_{\text{Na-Na}} \rangle$ by taking $z[d_1] = (d_1 - 1.66 \text{ \AA})/0.0882 \text{ \AA}$ and $z[\langle d_{\text{Na-Na}} \rangle] = (\langle d_{\text{Na-Na}} \rangle - 3.64)/0.164$ and assuming $\bar{\eta} \cong \eta$ and $\sigma_{\text{Na},300\text{K,sim}} \cong \sigma_{\text{Na},300\text{K}} = \frac{(z_{\text{Na}}F)^2 \rho_{\text{Na}}}{RT} D_{\text{Na},300\text{K}}$, where z_{Na} ($= +1$) is the valence for a Na-ion, and F and R denote the Faraday constant and the gas constant, respectively:

$$\sigma_{\text{Na},300\text{K,sim}}(d_1, \langle d_{\text{Na-Na}} \rangle) \equiv$$

$$(6.20 \times 10^6 \text{ S} \cdot \text{cm}^{-1}) (\rho_{\text{Na}} \text{ \AA}^3) 10^{\left(\frac{1}{1+e^{(-14.5 \text{ \AA}^{-1} d_1 + 7.70 \langle d_{\text{Na-Na}} \rangle - 4.527)}} - 2.82\right)/0.261}. \quad (3)$$

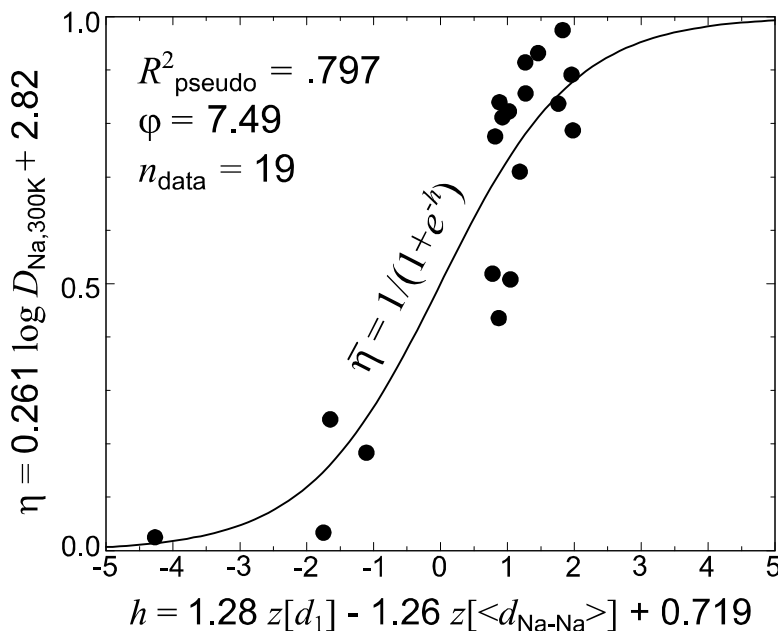


Fig. 2 Multivariate beta regression models with the highest pseudo-goodness-of-fit R^2_{pseudo} value given two descriptors allowed, wherein low- and high-performance samples are easily distinguishable in a binary-like manner. For the notations, Eqs. (2), (10)–(12) are referred to.

In previous studies, diffusion-pathway descriptors, including d_1 , have been identified as crucial indicators that contribute to decreased steric hindrance during ion migrations.^{60, 61} Meanwhile, the decrease in $\langle d_{\text{Na}-\text{ }} \rangle$ may imply the importance of Coulombic repulsion among Na-ions. Consequently, it can be inferred that a diffusion pathway characterized by decreased steric hindrance and shorter interstitial distances among Na-ions would result in the increase of $D_{\text{Na},300\text{K}}$. In Supplementary Note 3, we compare the descriptors for $D_{\text{Na},300\text{K}}$ in NASICONs and Na-ion sulfides.¹⁰

To construct a regression model that is readily interpretable, we further found secondary easily-accessible descriptors for $\sigma_{\text{Na},300\text{K}}$ ($\propto \rho_{\text{Na}} D_{\text{Na},300\text{K}}$) which involved transitioning from the primary descriptors ρ_{Na} , d_1 , and $\langle d_{\text{Na-N}} \rangle$. (Herein, the term “secondary” descriptors signify information given independently of structure, whereas “primary” descriptors pertain to the Na-ion diffusion pathways inherent in the NASICON structure.) For the purpose, we developed linear regression models as described in Supplementary Note 4, wherein ρ_{Na} , d_1 , and $\langle d_{\text{Na-Na}} \rangle$ were regressed with n and $\langle r_M \rangle$. In broad terms, it can be stated that n plays a pivotal role in the modulation of both ρ_{Na} and $\langle d_{\text{Na-Na}} \rangle$, whereas $\langle r_M \rangle$ exerts significant influence over d_1 . With Supplementary Eqs. (S6)–(S9), $\sigma_{\text{Na},300\text{K,sim}}$ was rewritten as a function of n and $\langle r_M \rangle$ from Eq. (3):

$$\sigma_{\text{Na},300\text{K,sim}}(n, \langle r_M \rangle) \equiv (6.20 \times 10^6 \text{ S} \cdot \text{cm}^{-1}) (0.00350n + 0.000527) 10^{\left(\frac{1}{1+\exp(8.02-5.86n+1.13n^2-5.22\text{\AA}^{-1}\langle r_M \rangle)}-2.82\right)/0.261}, \quad (4)$$

wherein the exponential part ($\propto D_{\text{Na},300\text{K}}$) would reach its zenith approximately $n = 2.59$. We plot $\sigma_{\text{Na},300\text{K,sim}}$ against n for different values of $\langle r_M \rangle$ in the range of [0.3, 0.5] Å in Fig. 3a. We estimated the overall goodnesses-of-fit for $\log_{10} \sigma_{\text{Na},300\text{K,sim}}$ against the trained dataset of $\log_{10} \sigma_{\text{Na},300\text{K}}$ (given in the single- T “long-time” diagnoses; listed in Table 1). The model exhibits a reasonable R^2 value of 0.694. It should be briefly noted that the beta regression model involving n and $\langle r_M \rangle$ only yielded the small size of $R_{\text{pseudo}}^2 = 0.243$, which can be attributed to the omission of nonlinear terms such as n^2 .

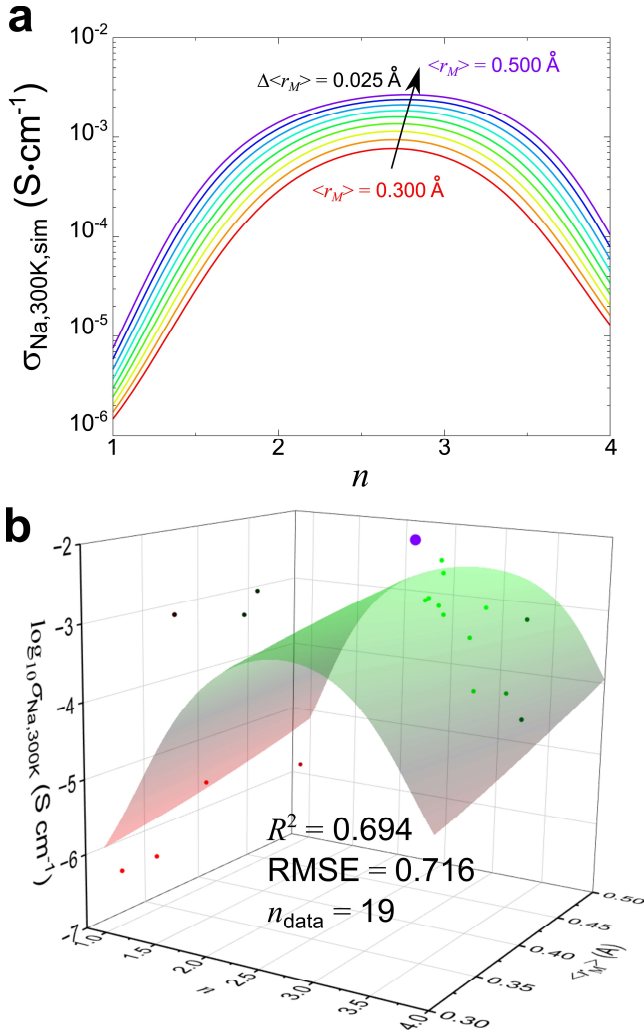


Fig. 3 **a** Simulated room-temperature Na-ion conductivity $\sigma_{\text{Na},300\text{K},\text{sim}}$ [see Eq. (4)] with varying Na-content n for given $\langle r_M \rangle$. Hue-color-scaled $\langle r_M \rangle$ are given in the range of [0.3, 0.5] Å with increment of 0.025 Å. **b** $\sigma_{\text{Na},300\text{K},\text{sim}}$ (represented by curved surface) compared with theoretical values $\sigma_{\text{Na},300\text{K}}$ listed in Table 1 (small dots) trained through the single- T “long-time” diagnoses (with $\Delta\tau = 1$ fs and $\tau = 1$ ns at $T = 300$ K). The values for R^2 and root mean square errors (RMSE) are also represented for $\log_{10} \sigma_{\text{Na},300\text{K}} = \log_{10} \sigma_{\text{Na},300\text{K},\text{sim}}$. The large purple dot represents the test case of $\text{Na}_{2.75}\text{Zr}_{1.75}\text{Nb}_{0.25}\text{Si}_2\text{PO}_{12}$ through the single- T “long-time” diagnosis: $\sigma_{\text{Na},300\text{K}} = 1.00 \times 10^{-2} \text{ S}\cdot\text{cm}^{-1}$.

Promising composition. We take a quinary chemical formula $\text{Na}_n\text{Zr}_{2-m'}M'_{m'}\text{Si}_{3-p}\text{P}_p\text{O}_{12}$ as our target, where the charge neutrality $[m' = (4 - p - n)/\{\nu(M') - 4\}]$ imposes a constraint for $\langle r_M \rangle$:

$$\langle r_M \rangle = \frac{1}{5} \left\{ \left(2 - \frac{4-p-n}{\nu(M')-4} \right) r_{\text{Zr}} + \frac{4-p-n}{\nu(M')-4} r_{M'} + (3-p)r_{\text{Si}} + pr_{\text{P}} \right\}; \quad (5)$$

it is given that $r_{\text{Zr}} = 0.72 \text{ \AA}$, $r_{\text{Si}} = 0.26 \text{ \AA}$, and $r_{\text{P}} = 0.17 \text{ \AA}$.⁵⁸ Thus, when a specific value of p is chosen alongside a particular selection of M' that yield $\nu(M')$ and $r_{M'}$, $\sigma_{\text{Na},300\text{K,sim}}$ can be simplified into a function of n . Under $p = 1$ as an example, we illustrate the variation of $\sigma_{\text{Na},300\text{K,sim}}$ concerning different values of n for various M' (24 in total) through Figs. 4a, 4b, 4c, and 4d. For $p = 1$, $\nu(M') = 4$, and $n = 3$ [as presented in Fig. 3c], it is given that

$$\sigma_{\text{Na},300\text{K,sim}}(m', r_{M'}) \equiv (1.06 \times 10^{-6} \text{ S} \cdot \text{cm}^{-1}) \exp \left[\frac{1}{0.113 + 0.0224 \exp(0.751m' - 1.04 \text{ \AA}^{-1} r_{M'} m')} \right]. \quad (6)$$

While Deng et al. previously proposed that the maximal value of $\sigma_{\text{Na},300\text{K}}$ is anticipated around at $n = 2.4$,⁶² we further notice that the optimization of $\sigma_{\text{Na},300\text{K,sim}}$ does not exclusively hinge on n considering the diverse array of M' selections.

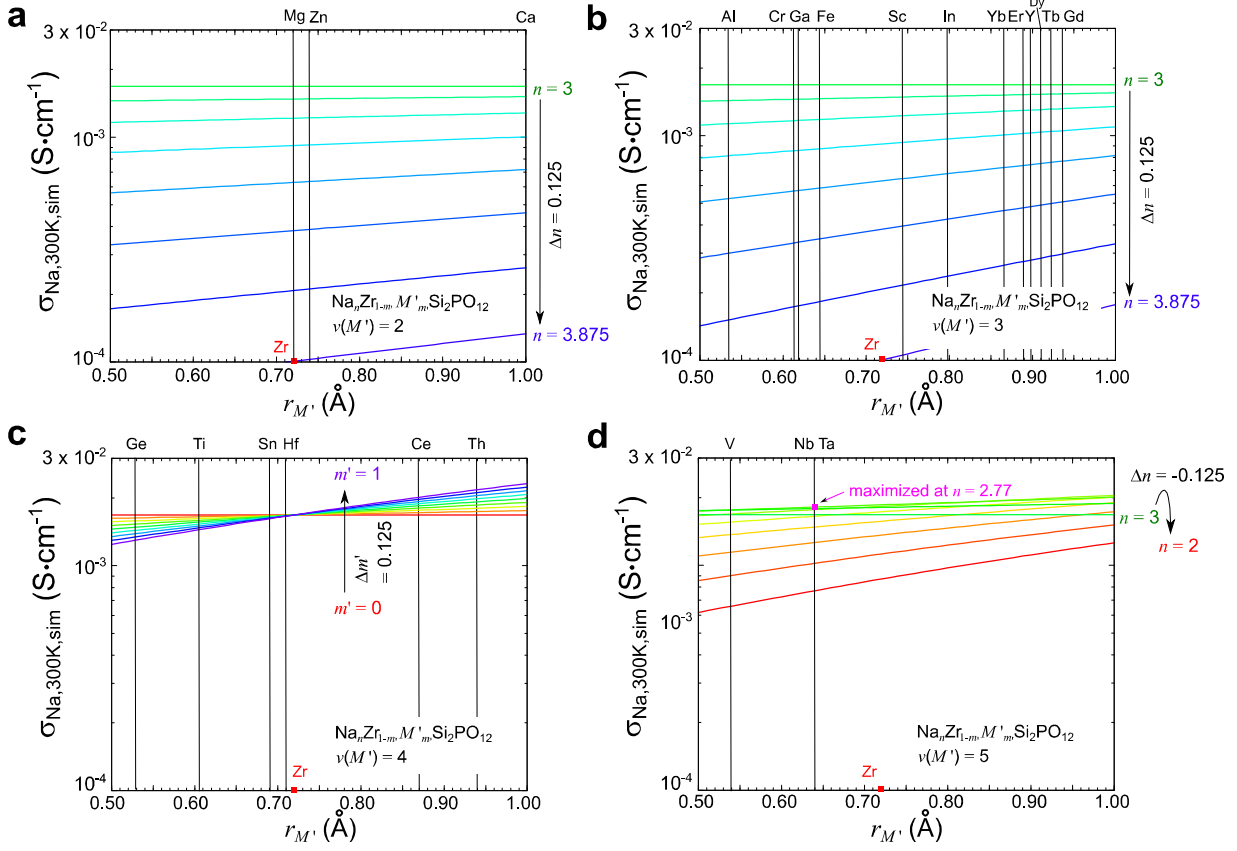


Fig. 4 $\sigma_{\text{Na},300\text{K},\text{sim}}$ varying with the Na-ion content n (or the dopant content m' : hue-color-scaled) and the ionic radius $r_{M'}$ of a dopant ion M' for $\text{Na}_n\text{Zr}_{2-m'}M'_{m'}\text{Si}_2\text{PO}_{12}$ given **a** divalent [$v(M') = 2$], **b** trivalent [$v(M') = 3$], **c** tetravalent [$v(M') = 4$], and **d** pentavalent [$v(M') = 5$] M' : 24 types of M' in total. $r_{M'}$ for various types of M' are represented by the vertical lines, and r_{Zr} is also denoted by red dots.⁷² The pink dot in **d** represents the case of the maximized $\sigma_{\text{Na},300\text{K},\text{sim}}$ across all M' except for Ce and Th: $M' = \text{Nb}$ and Ta and $n = 2.77$.

Herein, we focused on a selection of potential M' candidates while addressing two key considerations. First, among the 24 choices, $M' = \text{Nb}$, Ce , Ta , and Th were found competitive as depicted in Figs. 3c and 3d. Second, building upon the findings by Ouyang et al.,⁶³ $r_{M'} \cong r_{\text{Zr}} =$

0.72 Å would offer notable advantages in terms of structural stability and synthesis accessibility. Considering $r_{\text{Nb}} = 0.64$ Å, $r_{\text{Ce}} = 0.87$ Å, $r_{\text{Ta}} = 0.64$ Å, and $r_{\text{Th}} = 0.94$ Å, $M' = \text{Nb}$ and Ta emerge as particularly intriguing, with which $\sigma_{\text{Na},300\text{K,sim}}$ would be maximized around at $n = 2.77$: $\sigma_{\text{Na},300\text{K,sim}} = 1.82 \times 10^{-3} \text{ S} \cdot \text{cm}^{-1}$. Subsequently, we formulated a test composition, namely $\text{Na}_{2.75}\text{Zr}_{1.75}\text{Nb}_{0.25}\text{Si}_2\text{PO}_{12}$, with the anticipation that the scenario would follow a similar trend in the case of Ta. For the structure searches, we carried out Ewald summation sampling and geometry optimizations using DFT for $\text{Na}_{2.75}\text{Zr}_{1.75}\text{Nb}_{0.25}\text{Si}_2\text{PO}_{12}$, considering not only the monoclinic structure but also the rhombohedral structure.¹¹ Starting from the monoclinic configuration, $\text{Na}_{2.75}\text{Zr}_{1.75}\text{Nb}_{0.25}\text{Si}_2\text{PO}_{12}$ exhibited $E_{\text{hull}} = 6.49 \text{ meV} \cdot \text{atom}^{-1}$ indicating its high structural stability. Moreover, the free energy calculated through DFT for the monoclinic structures was found more stable by 3.52 meV·atom⁻¹ compared to the rhombohedral counterpart. Fig. 5a illustrate the crystal structure of $\text{Na}_{2.75}\text{Zr}_{1.75}\text{Nb}_{0.25}\text{Si}_2\text{PO}_{12}$ based on the initial monoclinic structure.

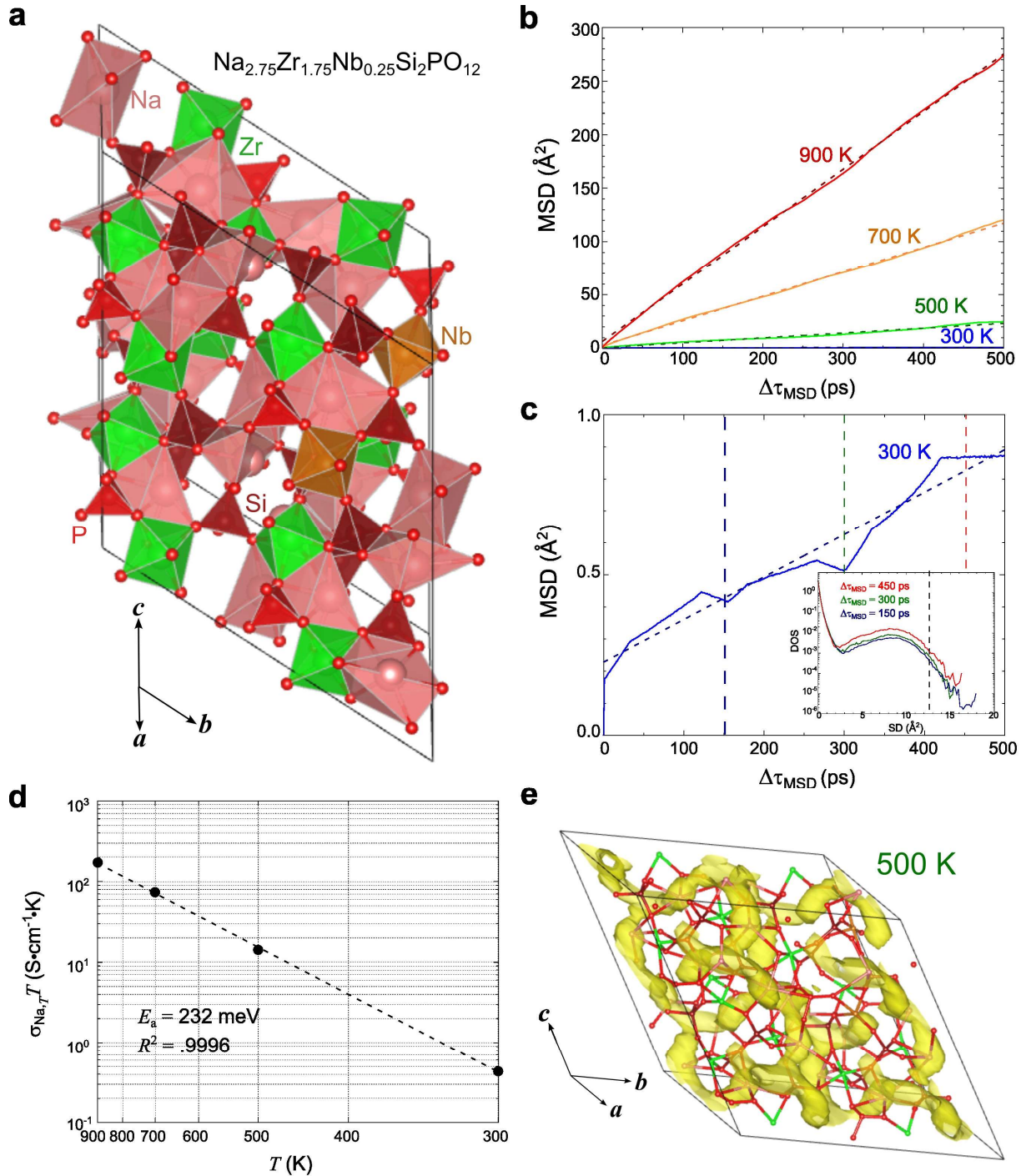


Fig. 5 **a** Crystal structure for $\text{Na}_{2.75}\text{Zr}_{1.75}\text{Nb}_{0.25}\text{Si}_2\text{PO}_{12}$. Pink, green, gold, dark red, and red polyhedra denote NaO_x , ZrO_6 , NbO_6 , SiO_4 , and PO_4 , respectively. The black arrows represent the lattice vectors. **b** The mean squared displacement (MSD) curves against sampled time intervals

$\Delta\tau_{\text{MSD}}$ given by the multi- T DFT-MD calculations (with $\Delta\tau = 1$ fs and $\tau = 600$ ps at $T = 300$, 500, 700, and 900 K). **c** The magnified view of the MSD curve for $T = 300$ K. In the inset, the density of states (DOS) for the trajectory samples, that is, squared displacement (SQ) data points across ensembles and times, where the area is normalized to 1. The blue, green, and red vertical dashed lines denote $\Delta\tau_{\text{MSD}} = 150$, 300, and 450 ps, respectively, which correspond to the DOS curves of the same colors in the inset. The black vertical dashed line in the inset denotes $\text{SD} = \langle d_{\text{Na-Na}} \rangle^2$, the squared Na-Na distance. In **b** and **c**, the dashed lines with slopes represent regressions against sampled time intervals $\Delta\tau_{\text{MSD}}$. **d** The Arrhenius plot in the $\sigma_{\text{Na},T}$ T - T domain with the calculated value of the Na-ion bulk activation energy E_a and the R^2 values. **e** The trajectory density plot at $T = 500$ K represented by yellow isosurfaces.

We proceeded with multi- T DFT-MD calculations to investigate $\sigma_{\text{Na},T}$ and E_a given the thermally-equilibrated unit cell volumes during the NpT pre-treatment stage. We represent the MSD curves in Figs. 5b and 5c. As indicated by Fig. 5c, there was the finite quantity of trajectory samples exhibiting squared displacements surpassing $\langle d_{\text{Na-Na}} \rangle^2$ at $T = 300$ K. In Fig. 5d, the corresponding Arrhenius plot in the $\sigma_{\text{Na},T}$ T - T domain is represented, wherein $\sigma_{\text{Na},300\text{K}}$ and E_a were estimated as 1.45×10^{-3} S·cm⁻¹ and 232 meV, respectively. It is noteworthy that $\sigma_{\text{Na},T}$ with $T = 500$, 700, and 900 K exhibit a nearly identical extrapolated value to that of $\sigma_{\text{Na},300\text{K}}$ given $R^2 = 0.9996$. This observation serves to partially validate the utilization of room-temperature DFT-MD calculations, particularly for high-performance samples. In Fig. 5e, we present the trajectory density plot given in $T = 500$ K, wherein the migration paths for Na-ions are intricately

interconnected within the bulk. The estimated values of $\sigma_{\text{Na},T}$, $D_{\text{Na},T}$, and R^2_{MSD} are also shown in Table 2.

Table 2 Values of Na-ion conductivities $\sigma_{\text{Na},T}$, self-diffusion coefficients $D_{\text{Na},T}$, and R -squared values R^2_{MSD} for the MSD curves regressed against sampled time intervals $\Delta\tau_{\text{MSD}}$, which were estimated by the multi- T DFT-MD calculations (with $\Delta\tau = 1$ fs and $\tau = 600$ ps at $T = 300$, 500, 700, and 900 K) for $\text{Na}_{2.75}\text{Zr}_{1.75}\text{Nb}_{0.25}\text{Si}_2\text{PO}_{12}$.

T (K)	$\sigma_{\text{Na},T}$ (S·cm ⁻¹)	$D_{\text{Na},T}$ (cm ² ·s ⁻¹)	R^2_{MSD}
300	1.45×10^{-3}	2.21×10^{-8}	.950
500	2.96×10^{-2}	7.55×10^{-7}	.978
700	1.05×10^{-1}	3.83×10^{-6}	.999
900	1.92×10^{-1}	8.96×10^{-6}	.999

Furthermore, to ensure a fair and consistent comparison with the values of $\sigma_{\text{Na},300\text{K}}$ and $D_{\text{Na},300\text{K}}$ presented in Table 1, which were determined through the single- T “long-time” diagnoses based on fixed unit cells optimized by using DFT without undergoing thermal equilibration, we carried out the same procedure for $\text{Na}_{2.75}\text{Zr}_{1.75}\text{Nb}_{0.25}\text{Si}_2\text{PO}_{12}$. Unexpectedly, the results yielded $\sigma_{\text{Na},300\text{K}} = 1.00 \times 10^{-2}$ S·cm⁻¹, visually depicted by the large purple dot in Fig. 3b. This outcome needs careful consideration, and its comprehensive discussion is given in detail in Supplementary Note 5.

Model revision for experimental cases. We carried out investigations to ascertain whether the easily-accessible descriptors n , n^2 , and $\langle r_M \rangle$ are adequate for accurately fitting the experimental values of $\sigma_{\text{Na},300\text{K}}$ as well. We meticulously collected all available experimental data points to our best knowledge, amounting to $n_{\text{data}} = 182$, which are exhaustively listed in Supplementary Table 3.^{15, 19, 20, 22, 23, 28-31, 34, 37, 41, 43-45, 47, 48, 53} We then refined the dataset by excluding compositions with Cr^{3+} , Fe^{3+} , Ce^{3+} , Gd^{3+} , and Yb^{3+} , where d or f electrons are partially filled. This exclusion narrowed down the dataset to $n_{\text{data}} = 140$. In our pursuit of capturing not only the high but also the low conductivity regime $\sigma_{\text{Na},300\text{K}} < 10^{-6} \text{ S}\cdot\text{cm}^{-1}$, which remains challenging to reconcile with Eq. (4), we introduced the probit function $p\sigma$ into our analytical framework:

$$\log_{10} p\sigma(n, \langle r_M \rangle) \equiv a_1 \log_{10} \left[\frac{1}{2} \left\{ 1 + \operatorname{erf} \left(\frac{a_2 + \sum_{j=1}^{df(j)} b_j [a_3 \log_{10} \sigma_{\text{Na},300\text{K},\text{sim}}(n, \langle r_M \rangle) + a_4]^{c_j}}{\sqrt{2}} \right) \right\} \right] + a_5, \quad (7)$$

where $df(j)$ represents the count of power functions of $\sigma_{\text{Na},300\text{K},\text{sim}}(n, \langle r_M \rangle)$, namely Eq. (4), incorporated into the model, and a_1 , a_2 , a_3 , a_4 , and a_5 serve as normalization factors for the error function; b_j and c_j are the only free parameters to the model, given $df(j)$. As $df(j)$ increases [$df(j) = 1$, 2 , and 3], the overall goodnesses-of-fit against the experimental values of $\log_{10} \sigma_{\text{Na},300\text{K}}$ were found as $R^2 = 0.687$, 0.718 , and 0.733 , respectively. At $df(j) = 2$, where R^2 approaches saturation, the coefficients in Eq. (7) were specified as follows: $a_1 = 12.6$, $a_2 = -3.01$, $a_3 = 0.308$, $a_4 = 1.79$, $a_5 = -14.8$, $(b_1, c_1) = (3.00, 0.0235)$, and $(b_2, c_2) = (1.30, 1.40)$. We plot $p\sigma(n, \langle r_M \rangle)$ with $df(j) = 2$ against n for different values of $\langle r_M \rangle$ in the range of $[0.3, 0.5] \text{ \AA}$ in Fig. 6a. The revised model exhibits a reasonable R^2 value of 0.718 , even when confronted with diverse synthesis techniques, distinct space groups, grain boundary effects,

ion-ion correlated effects, and other pertinent factors, as illustrated in Fig. 6b. This observation leads us to the conclusion that the development of a model for $\sigma_{\text{Na},300\text{K}}$ incorporating n , n^2 , and $\langle r_M \rangle$ is indeed feasible.

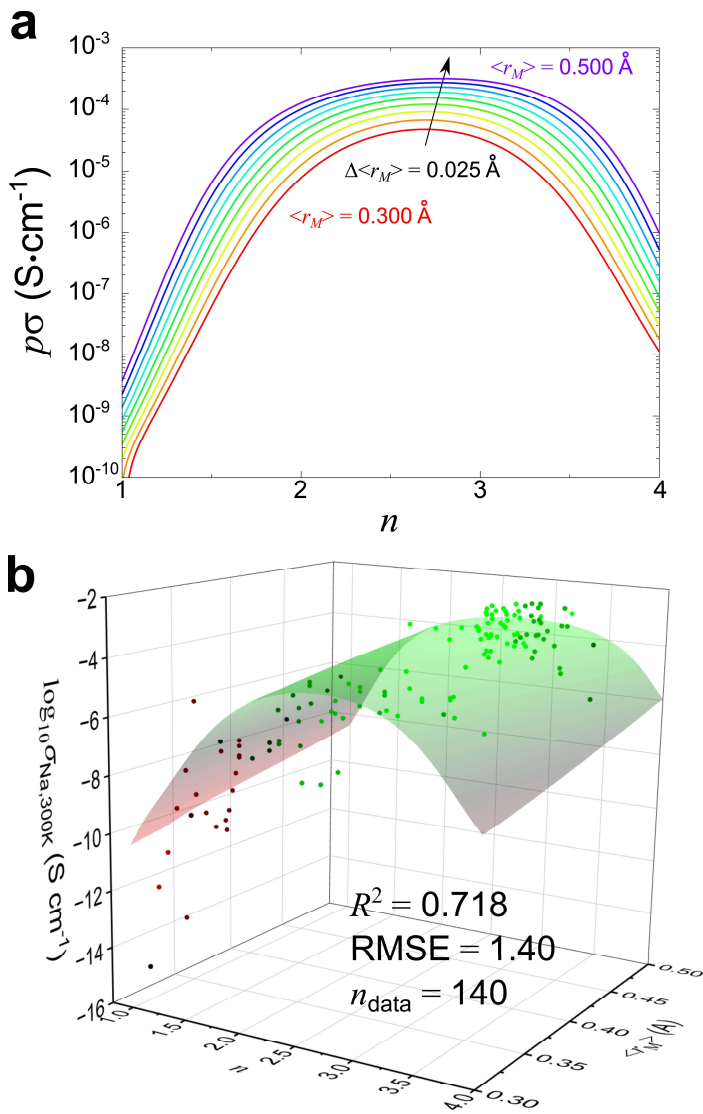


Fig. 6 **a** Simulated room-temperature Na-ion conductivity $p\sigma(n, \langle r_M \rangle)$ [see Eq. (7)] with varying Na-content n for given $\langle r_M \rangle$. Hue-color-scaled $\langle r_M \rangle$ are given in the range of [0.3, 0.5] Å with increment of 0.025 Å. **b** $p\sigma(n, \langle r_M \rangle)$ (represented by curved surface) compared with experimental values $\sigma_{\text{Na},300\text{K}}$ listed in Supplementary Table 3 (dots), illustrated with easily-accessible descriptors n and $\langle r_M \rangle$. The values for R^2 and root mean square errors (RMSE) are also represented for $\log_{10} \sigma_{\text{Na},300\text{K}} = \log_{10} p\sigma_{\text{Na},300\text{K},\text{sim}}$. Herein, compositions with Cr^{3+} , Fe^{3+} , Ce^{3+} , Gd^{3+} , and Yb^{3+} are excluded, where d or f electrons are partially filled: $n_{\text{data}} = 140$.

Summary and Outlook

This study employed DFT-MD to establish an explicit regression model for predicting $\sigma_{\text{Na},300\text{K}}$ within NASICON-type solid electrolytes for potential use in solid-state batteries. By using regression techniques including multivariate beta regression modelling, we successfully built a model with two easily-accessible descriptors only: n (and n^2 as well) and $\langle r_M \rangle$. This simplicity in the model's features suggests an efficient and resource-effective approach to predicting ion conductivity, making it potentially applicable to a wide range of materials. We also note that a closely related study by Wang et al., briefly discussed that the finding optimal value of $\sigma_{\text{Na},300\text{K}}$ may be possible with descriptors similar to ours, albeit rather in broad strokes.⁶⁴

This model led to the exploration of $\text{Na}_{2.75}\text{Zr}_{1.75}\text{Nb}_{0.25}\text{Si}_2\text{PO}_{12}$, as well. The material was found thermodynamically stable with $E_{\text{hull}} = 6.49 \text{ meV}\cdot\text{atom}^{-1}$. Subsequent multi- T DFT-MD calculations confirmed that this promising yet unexplored stable composition $\text{Na}_{2.75}\text{Zr}_{1.75}\text{Nb}_{0.25}\text{Si}_2\text{PO}_{12}$ may likely achieve $\sigma_{\text{Na},300\text{K}} > 10^{-3} \text{ S}\cdot\text{cm}^{-1}$. The result demonstrates the potential of this material as solid electrolytes in Na-ion-based solid-state batteries. Also, given the same ionic radii for Nb^{5+} and Ta^{5+} (0.64 \AA),⁵⁸ the case of $M' = \text{Ta}$ with the same Na-ion content is also worth consideration for the future study. Meanwhile, its revision successfully predicted the 140 experimental values of $\sigma_{\text{Na},300\text{K}}$ as well, demonstrating the robustness and applicability of the model to real-world scenarios.

Associated content

Supporting Information

The details of multivariate beta regression models and considered features (descriptor candidates), the mean squared displacement plots given by the single-temperature “long-time” diagnoses, the feature (descriptor candidates) dataset used for the multivariate beta regression modelling, the comparison of descriptors for $D_{\text{Na},300\text{K}}$ in NASICONs and Na-ion sulfides, the linear regressed models for the primary descriptors against the secondary ones, the experimental data for $\sigma_{\text{Na},300\text{K}}$ in the literature, and the results given in the single-temperature “long-time” diagnosis for $\text{Na}_{2.75}\text{Zr}_{1.75}\text{Nb}_{0.25}\text{Si}_2\text{PO}_{12}$.

Author information

Acknowledgments

This research was supported in part by MEXT as “Program for Promoting Research on the Supercomputer Fugaku” grant number JPMXP1020200301, Data Creation and Utilization Type Material Research and Development Project grant number JPMXP1121467561 and Materials Processing Science project (“Materealize”) grant number JPMXP0219207397, and by JSPS KAKENHI grant numbers JP21K14729, as well as JST through ALCA-SPRING grant number JPMJAL1301, GteX grant numbers JPMJGX23S2, and COI-NEXT grant number JPMJPF2016. The calculations were performed on the supercomputers at NIMS (Numerical Materials Simulator). Visualization for crystal structures was made with the VESTA software.⁶⁵ Plots were generated using gnuplot 5.4.⁶⁶

References

1. Takada, K. Progress and prospective of solid-state lithium batteries. *Acta Materialia* **2013**, *61* (3), 759-770. DOI: 10.1016/j.actamat.2012.10.034
2. Hayashi, A., Sakuda, A. & Tatsumisago, M. Development of sulfide solid electrolyte and interface formation processes for bulk-type all-solid-state Li and Na batteries. *Front. Energy Res.* **2016**, *4*, 25. DOI: 10.3389/fenrg.2016.00025
3. Zheng, F.; Kotobuki, M.; Song, S.; Lai, M. O.; Lu, L. Review on solid electrolytes for all-solid-state lithium-ion batteries. *J. Power Sources* **2018**, *389*, 198-213. DOI: 10.1016/j.jpowsour.2018.04.022
4. Ye, T.; Li, L.; Zhang, Y. Recent progress in solid electrolytes for energy storage devices. *Adv. Funct. Mater.* **2020**, *30* (29), 2000077. DOI: 10.1002/adfm.202000077
5. Liang, F.; Sun, Y.; Yuan, Y.; Huang, J.; Hou, M.; Lu, J. Designing inorganic electrolytes for solid-state Li-ion batteries: A perspective of LGPS and garnet. *Mater. Today*, **2021**, *50*, 418-441. DOI: 10.1016/j.mattod.2021.03.013
6. Hong, H. Y-P. Crystal structure and ionic conductivity of $\text{Li}_{14}\text{Zn}(\text{GeO}_4)_4$ and other new Li^+ superionic conductors. *Mater. Res. Bull.* **1978**, *13* (2), 117-124. DOI: 10.1016/0025-5408(78)90075-2
7. Murugan, R.; Thangadurai, V.; Weppner, W. Fast lithium ion conduction in garnet-type $\text{Li}_7\text{La}_3\text{Zr}_2\text{O}_{12}$. *Angew. Chem. Int. Ed.* **2007**, *46* (41), 7778-7781. DOI: 10.1002/anie.200701144

8. Kamaya, N.; Homma, K.; Yamakawa, Y.; Hirayama, M.; Kanno, R.; Yonemura, M.; Kamiyama, T.; Kato, Y.; Hama, S.; Kawamoto, K.; Mitsui, A. A lithium superionic conductor. *Nat. Mater.* **2011**, *10*, 682-686. DOI: 10.1038/nmat3066
9. Hayashi, A.; Masuzawa, N.; Yubuchi, S.; Tsuji, F.; Hotohama, C.; Sakuda, A.; Tatsumisago, M. A sodium-ion sulfide solid electrolyte with unprecedented conductivity at room temperature. *Nat. Comun.* **2019**, *10*, 5266. DOI: 10.1038/s41467-019-13178-2
10. Jang, S.-H.; Tateyama, Y.; Jalem, R. High-throughput data-driven prediction of stable high-performance Na-ion sulfide solid electrolytes. *Adv. Funct. Mater.* **2022**, *32* (48), 2206036. DOI: 10.1002/adfm.202206036
11. Hong, H. Y-P. Crystal structures and crystal chemistry in the system $\text{Na}_{1+x}\text{Zr}_2\text{Si}_x\text{P}_{3-x}\text{O}_{12}$. *Mater. Res. Bull.* **1976**, *11* (2), 173-182. DOI: 10.1016/0025-5408(76)90073-8
12. Goodenough, J. B.; Hong, H. Y-P.; Kafalas, J. A. Fast Na^+ -ion transport in skeleton structures. *Mater. Res. Bull.* **1976**, *11* (2), 203-220. DOI: 10.1016/0025-5408(76)90077-5
13. Li, C.; Li, R.; Liu, K.; Si, R.; Zhang, Z.; Hu, Y.-S. NaSICON: A promising solid electrolyte for solid-state sodium batteries. *Interdiscip. Mater.* **2022**, *1* (3), 396-416. DOI: 10.1002/idm2.12044
14. Avdeev, M. Crystal chemistry of NaSICONs: Ideal framework, distortion, and connection to properties. *Chem. Mater.* **2021**, *33* (19), 7620-7632. DOI: 10.1021/acs.chemmater.1c02695

15. Takahashi, T.; Kuwabara, K.; Shibata, M. Solid-state ionics - conductivities of Na^+ ion conductors based on NASICON. *Solid State Ion.* **1980**, *1* (3-4), 163-175. DOI: 10.1016/0167-2738(80)90001-6
16. Cherkaoui, F.; Viala, J. C.; Delmas, C.; Hagenmuller, P. Crystal chemistry and ionic conductivity of a new Nasicon-related solid solution $\text{Na}_{1+x}\text{Zr}_{2-x}\text{Mg}_x\text{PO}_4$. *Solid State Ion.* **1986**, *21* (4), 333-337. DOI: 10.1016/0167-2738(86)90195-5
17. Krok, F.; Kony, D.; Dygas, J. R.; Jakubowski, W.; Bogusz, W. On some properties of NASICON doped with MgO and CoO. *Solid State Ion.* **1989**, *36* (3-4), 251-254. DOI: 10.1016/0167-2738(89)90184-7
18. Slater, P. R.; Greaves, C. Synthesis and conductivities of sulfate/selenate phases related to Nasicon: $\text{Na}_xM^{''}(II)_xM^{'}(III)_{2-x}(\text{SO}_4)_{3-y}(\text{SeO}_4)_y$. *J. Solid State Chem.* **1993**, *107* (1), 12-18. DOI: 10.1006/jssc.1993.1317
19. Song, S.; Duong, H. M.; Korsunsky, A. M.; Hu, N.; Lu, L. A Na^+ superionic conductor for room-temperature sodium batteries. *Sci. Rep.* **2016**, *6*, 32330. DOI: 10.1038/srep32330
20. Lu, Y.; Alonso, J. A.; Yi, Q.; Lu, L.; Wang, Z. L.; Sun, C. A high-performance monolithic solid-state sodium battery with Ca^{2+} doped $\text{Na}_3\text{Zr}_2\text{Si}_2\text{PO}_{12}$ electrolyte. *Adv. Energy Mater.* **2019**, *9* (28), 1901205. DOI: 10.1002/aenm.201901205
21. Tillement, O.; Angenault, J.; Couturier, J. C.; Quarton, M. Mixed conductivity of the NASICON phase $\text{Na}_{2+x+y}\text{Zr}_{1-y}\text{Fe}^{II}_x\text{Fe}^{III}_{1-x+y}(\text{PO}_4)_3$. *Solid State Ion.* **1991**, *44* (3-4), 299-303. DOI: 10.1016/0167-2738(91)90022-4

22. Perthuis, H.; Colomban, Ph. Well densified NASICON type ceramics, elaborated using sol-gel process and sintering at low temperatures. *Mater. Res. Bull.* **1984**, *19* (5), 621-631. DOI: 10.1016/0025-5408(84)90130-2
23. Winand, J. M.; Rulmont, A.; Tarte, P. Ionic conductivity of the $\text{Na}_{1+x}M^{\text{III}}_x\text{Zr}_{2-x}(\text{PO}_4)_3$ systems ($M = \text{Al, Ga, Cr, Fe, Sc, In, Y, Yb}$). *J. Mater. Sci.* **1990**, *25*, 4008-4013. DOI: 10.1007/BF00582473
24. Saito, Y.; Ado, K.; Asai, T.; Kageyama, H.; Nakamura, O. Ionic conductivity of NASICON-type conductors $\text{Na}_{1.5}M_{0.5}\text{Zr}_{1.5}(\text{PO}_4)_3$ ($M: \text{Al}^{3+}, \text{Ga}^{3+}, \text{Cr}^{3+}, \text{Sc}^{3+}, \text{Fe}^{3+}, \text{In}^{3+}, \text{Yb}^{3+}, \text{Y}^{3+}$). *Solid State Ion.* **1992**, *58* (3-4), 327-331. DOI: 10.1016/0167-2738(92)90136-D
25. Maldonado-Manso, P.; Aranda, M. A. G.; Bruque, S.; Sanz, J.; Losilla, E. R. Nominal vs. actual stoichiometries in Al-doped NASICONs: A study of the $\text{Na}_{1.4}\text{Al}_{0.4}M_{1.6}(\text{PO}_4)_3$ ($M = \text{Ge, Sn, Ti, Hf, Zr}$) family. *Solid State Ion.* **2005**, *176* (17-18), 1613-1625. DOI: 10.1016/j.ssi.2005.04.009
26. de la Rouchère, M.; d'Yvoire, F.; Collin, G.; Comès, R.; Boilot, J. P. NASICON type materials - $\text{Na}_3M_2(\text{PO}_4)_3$ ($M = \text{Sc, Cr, Fe}$): Na^+ - Na^+ correlations and phase transitions. *Solid State Ion.* **1983**, *9-10* (2), 825-828. DOI: 10.1016/0167-2738(83)90096-6
27. Subramanian, M. A.; Rudolf, P. R.; Clearfield, A. The preparation, structure, and conductivity of scandium-substituted NASICONs. *J. Solid State Chem.* **1985**, *60* (2), 172-181. DOI: 10.1016/0022-4596(85)90109-4

28. Znaidi, L.; Launay, S.; Quarton, M. Crystal chemistry and electrical properties of $\text{Na}_{1+x}\text{ScNb}(\text{PO}_4)_3$ phases. *Solid State Ion.* **1997**, *93* (3-4), 273-277. DOI: 10.1016/S0167-2738(96)00558-9
29. Guin, M.; Tietz, F.; Guillon, O. New promising NASICON material as solid electrolyte for sodium-ion batteries: Correlation between composition, crystal structure and ionic conductivity of $\text{Na}_{3+x}\text{Sc}_2\text{Si}_x\text{P}_{3-x}\text{O}_{12}$. *Solid State Ion.* **2016**, *293* (1), 18-26. DOI: 10.1016/j.ssi.2016.06.005
30. Ma, Q.; Guin, M.; Naqash, S.; Tsai, C.-L.; Tietz, F.; Guillon, O. Scandium-substituted $\text{Na}_3\text{Zr}_2(\text{SiO}_4)_2(\text{PO}_4)$ prepared by a solution-assisted solid-state reaction method as sodium-ion conductors. *Chem. Mater.* **2016**, *28* (13), 4821-4828. DOI: 10.1021/acs.chemmater.6b02059
31. Delmas, C.; Viala, J.-C.; Olazcuaga, R.; Le Flem, G.; Hagenmuller, P.; Cherkaoui, F.; Brochu, R. Ionic conductivity in Nasicon-type phases $\text{Na}_{1+x}\text{Zr}_{2-x}\text{L}_x(\text{PO}_4)_3$ ($L = \text{Cr, In, Yb}$). *Solid State Ion.* **1981**, *3-4*, 209-214. DOI: 10.1016/0167-2738(81)90084-9
32. d'Yvoire, F.; Pintard-Scrépel, M.; Bretey, E.; de la Rochère, M. Phase transitions and ionic conduction in 3D skeleton phosphates $A_3M_2(\text{PO}_4)_3$: $A = \text{Li, Na, Ag, K}$; $M = \text{Cr, Fe}$. *Solid State Ion.* **1983**, *9-10* (2), 851-857. DOI: 10.1016/0167-2738(83)90101-7
33. Patoux, S.; Rousse, G.; Leriche, J.-B.; Masquelier, C. Structural and electrochemical studies of rhombohedral $\text{Na}_2\text{Ti}M(\text{PO}_4)_3$ and $\text{Li}_{1.6}\text{Na}_{0.4}\text{Ti}M(\text{PO}_4)_3$ ($M = \text{Fe, Cr}$) phosphates. *Chem. Mater.* **2003**, *15* (10), 2084-2093. DOI: 10.1021/cm020479p
34. Fujitsu, S.; Nagai, M.; Kanazawa, T.; Yasui, I. Conduction paths in sintered ionic conductive material $\text{Na}_{1+x}\text{Y}_x\text{Zr}_{2-x}(\text{PO}_4)_3$. *Mater. Res. Bull.* **1981**, *16* (10), 1299-1309. DOI: 10.1016/0025-5408(81)90101-X

35. Miyajima, Y.; Miyoshi, T.; Tamaki, J.; Matsuoka, M.; Yamamoto, Y.; Masquelier, C.; Tabuchi, M.; Saito, Y.; Kageyama, H. Solubility range and ionic conductivity of large trivalent ion doped $\text{Na}_{1+x}\text{M}_x\text{Zr}_{2-x}\text{P}_3\text{O}_{12}$ (M : In, Yb, Er, Y, Dy, Tb, Gd) solid electrolytes. *Solid State Ion.* **1999**, *124* (3-4), 201-211. DOI: 10.1016/S0167-2738(99)00116-2
36. Smirnova, O. A.; Fuentes, R. O.; Figueiredo, F.; Kharton, V. V.; Marques, F. M. B. Stability and thermal expansion of Na^+ -Conducting Ceramics. *J. Electroceram.* **2003**, *11*, 179-189. DOI: 10.1023/B:JECR.0000026373.56703.b0
37. Fuentes, R. O.; Figueiredo, F. M.; Soares, M. R.; Marques, F. M. B. Submicrometric NASICON ceramics with improved electrical conductivity obtained from mechanically activated precursors. *J. Eur. Ceram. Soc.* **2005**, *25* (4), 455-462. DOI: 10.1016/j.jeurceramsoc.2004.02.019
38. Losilla, E. R.; Aranda, M. A. G.; Bruque, S.; Sanz, J.; París, M. A.; Campo, J.; West, A. R. Sodium mobility in the NASICON Series $\text{Na}_{1+x}\text{Zr}_{2-x}\text{In}_x(\text{PO}_4)_3$. *Chem. Mater.* **2000**, *12* (8), 2134-2142. DOI: 10.1021/cm000122q
39. Wang, W.; Wang, S.; Rao, L.; Lu, Z.; Yu, X. Study of $\text{Na}_{1+x+y}\text{Zr}_{2-y}\text{Nd}_y\text{Si}_x\text{P}_{3-x}\text{O}_{12}$ fast ion conductors. *Solid State Ion.* **1988**, *28-30* (1), 424-426. DOI: 10.1016/S0167-2738(88)80076-6
40. Bentzen, J. J.; Nicholson, P. S. The preparation and characterization of dense, highly conductive $\text{Na}_5\text{GdSi}_4\text{O}_{12}$ nasicon (NGS). *Mater. Res. Bull.* **1980**, *15* (12), 1737-1745. DOI: 10.1016/0025-5408(80)90191-9
41. Khakpour, Z. Influence of M : Ce^{4+} , Gd^{3+} and Yb^{3+} substituted $\text{Na}_{3+x}\text{Zr}_{2-x}\text{M}_x\text{Si}_2\text{PO}_{12}$ solid NASICON electrolytes on sintering, microstructure and conductivity. *Electrochim. Acta.* **2016**, *196*, 337-347. DOI: 10.1016/j.electacta.2016.02.199

42. Miyajima, Y.; Saito, Y.; Matsuoka, M.; Yamamoto, Y. Ionic conductivity of NASICON-type $\text{Na}_{1+x}M_x\text{Zr}_{2-x}\text{P}_3\text{O}_{12}$ (M : Yb, Er, Dy). *Solid State Ion.* **1996**, *84* (1-2), 61-64. DOI: 10.1016/S0167-2738(96)83006-2
43. Zahir, M.; Olazcuaga, R.; Hagenmuller, P. Crystal chemistry and ionic conductivity in Nasicon-type phases $\text{Na}_{1+x}\text{Zr}_{2-x}\text{Yb}_x(\text{AsO}_4)_3$ with $0 \leq x \leq 0.45$. *Mater. Lett.* **1984**, *2* (3), 234-236. DOI: 10.1016/0167-577X(84)90032-6
44. Cava, R. J.; Vogel, E. M.; Johnson Jr., D. W. Effect of homovalent framework cation substitutions on the sodium ion conductivity in $\text{Na}_3\text{Zr}_2\text{Si}_2\text{PO}_{12}$. *J. Am. Ceram. Soc.* **1982**, *65* (9), c157-c159. DOI: 10.1111/j.1151-2916.1982.tb10526.x
45. Winand, J. M.; Rulmont, A.; Tarte, P. Nouvelles solutions solides $L^1(M^{IV})_{2-x}(N^{IV})_x(\text{PO}_4)_3$ ($L = \text{Li}, \text{Na}$ $M, N = \text{Ge}, \text{Sn}, \text{Ti}, \text{Zr}, \text{Hf}$) synthèse et étude par diffraction x et conductivité ionique. *J. Solid State Chem.* **1991**, *93* (2), 341-349. DOI: 10.1016/0022-4596(91)90308-5
46. Shimazu, K.; Yamamoto, Y.; Saito, Y.; Nakamura, O. Electrical conductivity and Ti^{4+} ion substitution range in NASICON system. *Solid State Ion.* **1995**, *79*, 106-110. DOI: 10.1016/0167-2738(95)00038-8
47. Yue, Y.; Pang, W. Hydrothermal synthesis and characterization of $\text{NaSn}_2(\text{PO}_4)_3$. *J. Mater. Sci. Lett.* **1992**, *11*, 148-149. DOI: 10.1007/BF00724673
48. Vogel, E. M.; Cava, R. J.; Rietman, E. Na^+ ion conductivity and crystallographic cell characterization in the Hf-nasicon system $\text{Na}_{1+x}\text{Hf}_2\text{Si}_x\text{P}_{3-x}\text{O}_{12}$. *Solid State Ion.* **1984**, *14* (1), 1-6. DOI: 10.1016/0167-2738(84)90002-X

49. Leclaire, A.; Borel, M. M.; Grandin, A.; Raveau, B. A niobium phosphate with a nasicon structure: $\text{Na}_{0.5}\text{Nb}_2(\text{PO}_4)_3$. *Mater. Res. Bull.* **1991**, *26* (2-3), 207-211. DOI: 10.1016/0025-5408(91)90011-A
50. Bennouna, L.; Arsalane, S.; Brochu, R.; Lee, M. R.; Chassaing, J.; Quarton, M. Spécificités des ions Nb^{IV} et Mo^{IV} dans les monophosphates de type Nasicon. *J. Solid State Chem.* **1995**, *114* (1), 224-229. DOI: 10.1006/jssc.1995.1032
51. Veríssimo, C.; Garrido, F. M. S.; Alves, O. L.; Calle, P.; Martínez-Juárez, A.; Iglesias, J. E.; Rojo, J. M. Ionic conductivity and structural characterization of $\text{Na}_{1.5}\text{Nb}_{0.3}\text{Zr}_{1.5}(\text{PO}_4)_3$ with NASICON-type structure. *Solid State Ion.* **1997**, *100* (1-2), 127-134. DOI: 10.1016/S0167-2738(97)00307-X
52. Liu, Y.; Liu, L.; Peng, J.; Zhou, X.; Liang, D.; Zhao, L.; Su, J.; Zhang, B.; Li, S.; Zhang, N.; Ma, Q.; Tietz, F. A niobium-substituted sodium superionic conductor with conductivity higher than 5.5 mScm^{-1} prepared by solution-assisted solid-state reaction method. *J. Power Sources*, **2022**, *518*, 230765. DOI: 10.1016/j.jpowsour.2021.230765
53. Stainer, F.; Gadermaier, B.; Kügerl, A.; Ladenstein, L.; Hogrefe, K.; Wilkening, H. M. R. Fast Na^+ Ion Dynamics in the Nb^{5+} Bearing NaSICON $\text{Na}_{3+x-z}\text{Nb}_z\text{Zr}_{2-z}\text{Si}_{2+x}\text{P}_{1-x}\text{O}_{12}$ as Probed by ^{23}Na NMR and Conductivity Spectroscopy. *Solid State Ion.* **2023**, *395*, 116209. DOI: 10.1016/j.ssi.2023.116209.
54. Jang, S.-H.; Jalem, R.; Tateyama, Y. *EwaldSolidSolution*: a high-throughput application to quickly sample stable site arrangements for ionic solid solutions. *J. Phys. Chem. A* **2023**, *127* (27), 5734-5744. DOI: 10.1021/acs.jpca.3c00076

55. Kieschnick, R.; McCullough, B. D. Regression analysis of variates observed on (0, 1): percentages, proportions and fractions. *Stat. Modelling* **2003**, *3* (3), 193-213. DOI: 10.1191/1471082X03st053oa
56. Ferrari, S.; Cribari-Neto, F. Beta regression for modelling rates and proportions. *J. Appl. Stat.* **2004**, *31* (7), 799-815. DOI: 10.1080/0266476042000214501
57. Cribari-Neto, F.; Zeileis, A. Beta regression in R. *J. Stat. Softw.* **2010**, *34* (2), 1-24. DOI: 10.18637/jss.v034.i02
58. Shannon, R. D. Revised effective ionic radii and systematic studies of interatomic distances in halides and chalcogenides. *Acta Crystallogr.* **1976**, *A32*, 751-767. DOI: 10.1107/S0567739476001551
59. Lunghammer, S.; Ma, Q.; Rettenwander, D.; Hanzu, I.; Tietz, F.; Wilkening, H. M. R. Bulk and grain-boundary ionic conductivity in sodium zirconophosphosilicate $\text{Na}_3\text{Zr}_2(\text{SiO}_4)_2\text{PO}_4$ (NASICON). *Chem. Phys. Lett.* **2018**, *701*, 147-150. DOI: 10.1016/j.cplett.2018.04.037
60. Jalem, R.; Hayashi, A.; Tsuji, F.; Sakuda, A.; Tateyama, Y. First-principles calculation study of Na^+ superionic conduction mechanism in W- and Mo-doped Na_3SbS_4 solid electrolytes. *Chem. Mater.* **2020**, *32* (19), 8373-8381. DOI: 10.1021/acs.chemmater.0c02318
61. Jalem, R.; Gao, B.; Tian, H.-K.; Tateyama, Y. Theoretical study on stability and ion transport property with halide doping of Na_3SbS_4 electrolyte for all-solid-state batteries. *J. Mater. Chem. A* **2020**, *10*, 2235-2248. DOI: 10.1039/D1TA07292G

62. Deng, Z.; Mishra, T. P.; Mahayoni, E.; Ma, Q.; Tieu, A. J. K.; Guillon, O.; Chotard, J.-N.; Seznec, V.; Cheetham, A. K.; Masquelier, C.; Gautam, G. S.; Canepa, P. Fundamental investigations on the sodium-ion transport properties of mixed polyanion solid-state battery electrolytes. *Nat. Commun.* **2022**, *13*, 4470. DOI: 10.1038/s41467-022-32190-7
63. Ouyang, B.; Wang, J.; He, T.; Bartel, C. J.; Huo, H.; Wang, Y.; Lacivita, V.; Kim, H.; Ceder, G. Synthetic accessibility and stability rules of NASICONs. *Nat. Commun.* **2021**, *12*, 5752. DOI: 10.1038/s41467-021-26006-3
64. Wang, J.; He, T.; Yang, X.; Cai, Z.; Wang, Y.; Lacivita, V.; Kim, H.; Ouyang, B.; Ceder, G. Design principles for NASICON super-ionic conductors. *Nat. Commun.* **2023**, *14*, 5210. DOI: 10.1038/s41467-023-40669-0
65. Momma, K.; Izumi, F. VESTA 3 for three-dimensional visualization of crystal, volumetric and morphology data. *J. Appl. Crystallogr.* **2011**, *44*, 1272-1276. DOI: 10.1107/S0021889811038970
66. Williams, T.; Kelley, C. *gnuplot 5.4: An interactive plotting program*, 2020.
http://www.gnuplot.info/docs_5.4/Gnuplot_5_4.pdf (accessed 2024-01-17).
67. Blöchl, P. E. Projector augmented-wave method. *Phys. Rev. B* **1994**, *50* (24), 17953-17979.
DOI: 10.1103/PhysRevB.50.17953
68. Perdew, J. P.; Burke, K.; Ernzerhof, M. Generalized gradient approximation made simple. *Phys. Rev. Lett.* **1996**, *77* (18), 3865-3868. DOI: 10.1103/PhysRevLett.77.3865

69. Kresse, G.; Furthmüller, J. Efficiency of ab-initio total energy calculations for metals and semiconductors using a plane-wave basis set. *Comp. Mater. Sci.* **1996**, *6* (1), 15-50. DOI: 10.1016/0927-0256(96)00008-0
70. Kresse, G.; Furthmüller, J. Efficient iterative schemes for ab initio total-energy calculations using a plane-wave basis set. *Phys. Rev. B* **1996**, *54* (16), 11169-11186. DOI: 10.1103/PhysRevB.54.11169
71. Kresse, G.; Joubert, D. From ultrasoft pseudopotentials to the projector augmented-wave method. *Phys. Rev. B* **1999**, *59* (3), 1758-1775. DOI: 10.1103/PhysRevB.59.1758
72. Monkhorst, H. J.; Pack, J. D. Special points for Brillouin-zone integrations. *Phys. Rev. B* **1976**, *13* (12), 5188-5192. DOI: 10.1103/PhysRevB.13.5188
73. Ong, S. P.; Wang, L.; Kang, B.; Ceder, G. The Li-Fe-P-O₂ phase diagram from first principles calculations. *Chem. Mater.* **2008**, *20* (5), 1798-1807. DOI: 10.1021/cm702327g
74. Ong, S. P.; Jain, A.; Hautier, G.; Kang, B.; Ceder, G. Thermal stabilities of delithiated olivine MPO₄ (M=Fe, Mn) cathodes investigated using first principles calculations. *Electrochem. commun.* **2020**, *12* (3), 427-430. DOI: 10.1016/j.elecom.2010.01.010
75. Nosé, S. A unified formulation of the constant temperature molecular dynamics methods. *J. Chem. Phys.* **1984**, *81* (1), 511-519. DOI: 10.1063/1.447334
76. Hoover, W. G. Canonical dynamics: Equilibrium phase-space distributions. *Phys. Rev. A* **1985**, *31* (3), 1695-1697. DOI: 10.1103/PhysRevA.31.1695

77. Smithson, M.; Verkuilen, J. A better lemon squeezer? Maximum-likelihood regression with beta-distributed dependent variables. *Psychol. Methods*, **2006**, 11(1), 54-71. DOI: 10.1037/1082-989X.11.1.54
78. *The R Project for Statistical Computing*. <https://www.R-project.org/> (accessed 2023-08-24).
79. Zeileis, A.; Cribari-Neto, F.; Gruen, B.; Kosmidis, I.; Simas, A. B.; Rocha, A. V. *Package 'betareg'*, 2022. <https://cran.r-project.org/web/packages/betareg/betareg.pdf> (accessed 2023-08-24).
80. Willems, T. F.; Rycroft, C. H.; Kazi, M.; Meza, J. C.; Haranczyk, M. Algorithms and tools for high-throughput geometry-based analysis of crystalline porous materials. *Microporous Mesoporous Mater.* **2012**, 149 (1), 134-141. DOI: 10.1016/j.micromeso.2011.08.020
81. Ongari, D.; Boyd, P. G.; Barthel, S.; Witman, M.; Haranczyk, M.; Smit, B. Accurate characterization of the pore volume in microporous crystalline materials. *Langmuir* **2017**, 33 (51), 14529-14538. DOI: 10.1021/acs.langmuir.7b01682
82. Parrinello, M.; Rahman, A. Crystal structure and pair potentials: a molecular-dynamics study. *Phys. Rev. Lett.* **1980**, 45 (14), 1196-1199. DOI: 10.1103/PhysRevLett.45.1196
83. Parrinello, M.; Rahman, A. Polymorphic transitions in single crystals: a new molecular dynamics method. *J. Appl. Phys.* **1981**, 52 (12), 7182-7190. DOI: 10.1063/1.328693

Methods

Site arrangement sampling. Using EwaldSolidSolution,⁵⁴ we performed Ewald summation sampling starting from the monoclinic structure $\text{Na}_3\text{Zr}_2\text{Si}_2\text{PO}_{12}$ with $C2/c$ symmetry that was determined experimentally.¹¹ By expanding the primitive cell, we created a $1 \times 2 \times 2$ supercell $\text{Na}_{32}^+\text{Zr}_{16}^{4+}\text{Si}_{16}^{4+}\text{P}_8^{5+}\text{O}_{96}^{2-}$, considering the presence of 8 excess Na-ion sites identified by a large Debye-Waller factor. Here, the lattice constants were given as $a = 9.0062 \text{ \AA}$, $b = 18.012 \text{ \AA}$, $c = 18.410 \text{ \AA}$, $\alpha = \beta = 61.308^\circ$, and $\gamma = 60.168^\circ$. While maintaining the number of O-ion sites (96), we randomly generated 957,600 to 3,783,780 site arrangements for each case of $\text{Na}_nM_mM'_m\text{Si}_{3-p-a}\text{P}_p\text{As}_a\text{O}_{12}$ by modifying $\text{Na}_{32}^+\text{Zr}_{16}^{4+}\text{Si}_{16}^{4+}\text{P}_8^{5+}\text{O}_{96}^{2-}$ to $\text{Na}_{8n}^+M_{8m}M'_{8m'}\text{Si}_{24-8p-8a}^{4+}\text{P}_{8p}^{5+}\text{As}_{8a}^{5+}\text{O}_{96}^{2-}$, wherein the total number of ion sites ranged from 144 to 166.

Geometry optimization. Following the site arrangement sampling, the five most stable site arrangement samples for each case were subjected to DFT geometry optimizations using the Vienna Ab Initio Simulation Package (VASP). We employed the generalized gradient approximation (GGA) and the projector augmented wave (PAW) method basis set.⁶⁷⁻⁷¹ The geometry optimizations included both site positions and lattice constants. Monkhorst-Pack \mathbf{k} -grids were set at $2 \times 2 \times 2$,⁷² and the kinetic energy cutoff of 520 eV was used. Convergence criteria of $< 0.01 \text{ eV}\cdot\text{\AA}^{-1}$ for forces and $< 10^{-5} \text{ eV}\cdot\text{atom}^{-1}$ for energy were applied. Some pseudopotentials included semicore electrons as valence states for specific elements: Ca, Sc, and Zr (semicore s electrons); Na, Mg, Ti, Nb, and Ta (p); and Ga, Ge, In, and Sn (d). For the other elements, standard pseudopotential forms were employed. Then, the lowest-energy structure sample for each investigated composition was selected for subsequent DFT-MD calculations, wherein we

calculated E_{hull} for all the samples by using the Computational Phase Diagram App provided by MaterialsProject.org^{73, 74} to verify their thermodynamic (meta)stability.

DFT-MD for data training. The single- T “long-time” diagnoses were carried out at $T = 300$ K given the geometry-optimized cell structures described above. First, a total of 10,000 DFT-MD steps (10 ps) were performed to ensure thermal equilibrations by using the Nosé-Hoover thermostat (NVT ensemble) implemented in VASP.^{75, 76} Subsequently, DFT-MD production runs were executed for trajectory sampling over $\tau = 1$ ns (NVT). Throughout the DFT-MD calculations, $\Delta\tau = 1$ fs, a $1 \times 1 \times 1$ \mathbf{k} -grid (that is, Γ only), and a kinetic energy cutoff of 400 eV were employed. The pseudopotentials were used in their standard forms except for Ca and Zr (with semicore s electrons) and Nb (p), and the calculations were performed using the GGA and the PAW method basis set.⁶⁷⁻⁷¹

From the sampled trajectories, the Na-ion self-diffusion coefficients $D_{\text{Na},T} = M_s/(2d)$ at T were estimated by carrying out regression analyses on the diffusive (linear) regime of the mean squared displacement (MSD) curves against sampled time intervals $\Delta\tau_{\text{MSD}}$, up to $\Delta\tau_{\text{MSD}} = 800$ ps; $D_{\text{Na},T}$ was obtained as the slope M_s of the MSD- $\Delta\tau_{\text{MSD}}$ regression line at T , considering the three-dimensional nature of Na-ion diffusion ($d = 3$). We also estimated R -squared values R^2_{MSD} for the MSD curves regressed against $\Delta\tau_{\text{MSD}}$. Then, the Na-ion ionic conductivity $\sigma_{\text{Na},T}$ at T is estimated by using the Nernst-Einstein equation

$$\sigma_{\text{Na},T} = \frac{(z_{\text{Na}}F)^2 \rho_{\text{Na}}}{RT} D_{\text{Na},T}, \quad (9)$$

where z_{Na} ($= +1$) is the valence for a Na-ion, ρ_{Na} is the Na-ion density, and F and R denote the Faraday constant and the gas constant, respectively.

Multivariate beta regression modelling. The goal is to find a beta regression model h whose sigmoid function response $\bar{\eta}$ well-fits the performance scores η for $\log_{10} D_{\text{Na},300\text{K}}$:

$$h = c + \sum_{i=1}^{df} c(x_i)z[x_i], \quad (10)$$

$$\bar{\eta} = 1/(1 + e^{-h}), \quad (11)$$

and

$$\eta = \frac{1}{n_{\text{data}}} \left\{ \frac{\log_{10} D_{\text{Na},300\text{K}} - \text{mi}}{\max[\log_{10} D_{\text{Na},300\text{K}}] - \min[\log_{10} D_{\text{Na},300\text{K}}]} (n_{\text{data}} - 1) + \frac{1}{2} \right\}, \quad (12)$$

where x_i , $z[x_i]$, and $c(x_i)$ ($i = \text{integer}$), c , df , and n_{data} denote the independent variables (that is, features considered as descriptor candidates), their z -scored values, and their coefficients, the constant term, the maximum number of taken x_i , i.e., the degree of freedom, and the number of data for $\log_{10} D_{\text{Na},300\text{K}}$, respectively. Eq. (4) was taken in that the target dependent variable in beta regression analysis is scaled in the range of (0,1), as introduced first by Smithson and Verkuilen.⁷⁷

While we leave the detailed descriptions of the maximum likelihood estimation and the pseudo-goodness-of-fit R^2_{pseudo} for the exhaustive search of the possible multivariate beta regression models in Supplementary Note 2, we briefly note that the R-package betareg was used for the analyses,^{57, 78, 79} and that the Zeo++ package was used for the three descriptors d_0 , d_1 , and V_p by referring to the Shannon ionic radii for ion sites.^{58, 80, 81}

DFT-MD for test dataset. The multi- T DFT-MD calculations were carried out at $T = 300, 500, 700$, and 900 K. First, a total of 40,000 DFT-MD steps (40 ps) were performed to achieve thermal and volume equilibrations by using the Langevin thermostat with the Parinello-

Rahman algorithm (NpT ensemble) implemented in VASP.^{82, 83} During this process, the averaged lattice constants were calculated over the last 10,000 DFT-MD steps (30 - 40 ps) to account for the thermally induced cell volume expansion. Subsequently, with the averaged lattice constants, thermal equilibration runs were repeated for 10,000 DFT-MD steps (10 ps) under the Nosé-Hoover thermostat (NVT). Finally, product runs were carried out afterwards for trajectory sampling over $\tau = 600$ ps (NVT). Meanwhile, the choices of $\Delta\tau$, the \mathbf{k} -grid, the kinetic energy cutoff, and the pseudopotentials and the post-process for $D_{\text{Na},T}$ and $\sigma_{\text{Na},T}$ were common to those of the DFT-MD for data training. $D_{\text{Na},T}$ were estimated by carrying out regression analyses on MSD curves against sampled time intervals $\Delta\tau_{\text{MSD}}$, up to $\Delta\tau_{\text{MSD}} = 500$ ps.

Supplementary Information

Predicting room-temperature conductivity of Na-ion super ionic conductors with the minimal number of easily-accessible descriptors

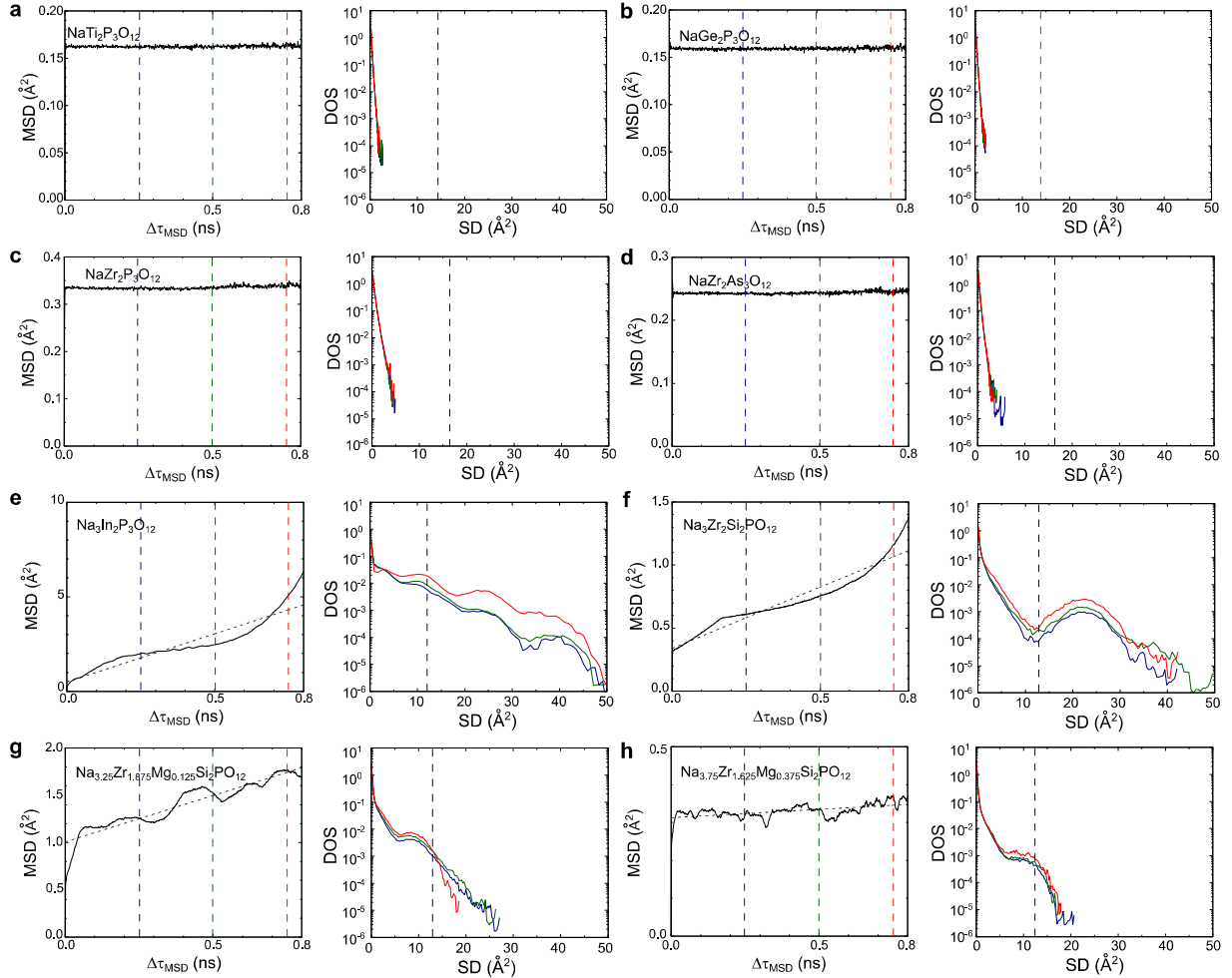
Seong-Hoon Jang,^{1,2} Randy Jalem², and Yoshitaka Tateyama^{2,3}*

¹ Institute for Materials Research, Tohoku University, 2-1-1 Katahira, Aoba-ku, Sendai, 980-8577, Japan

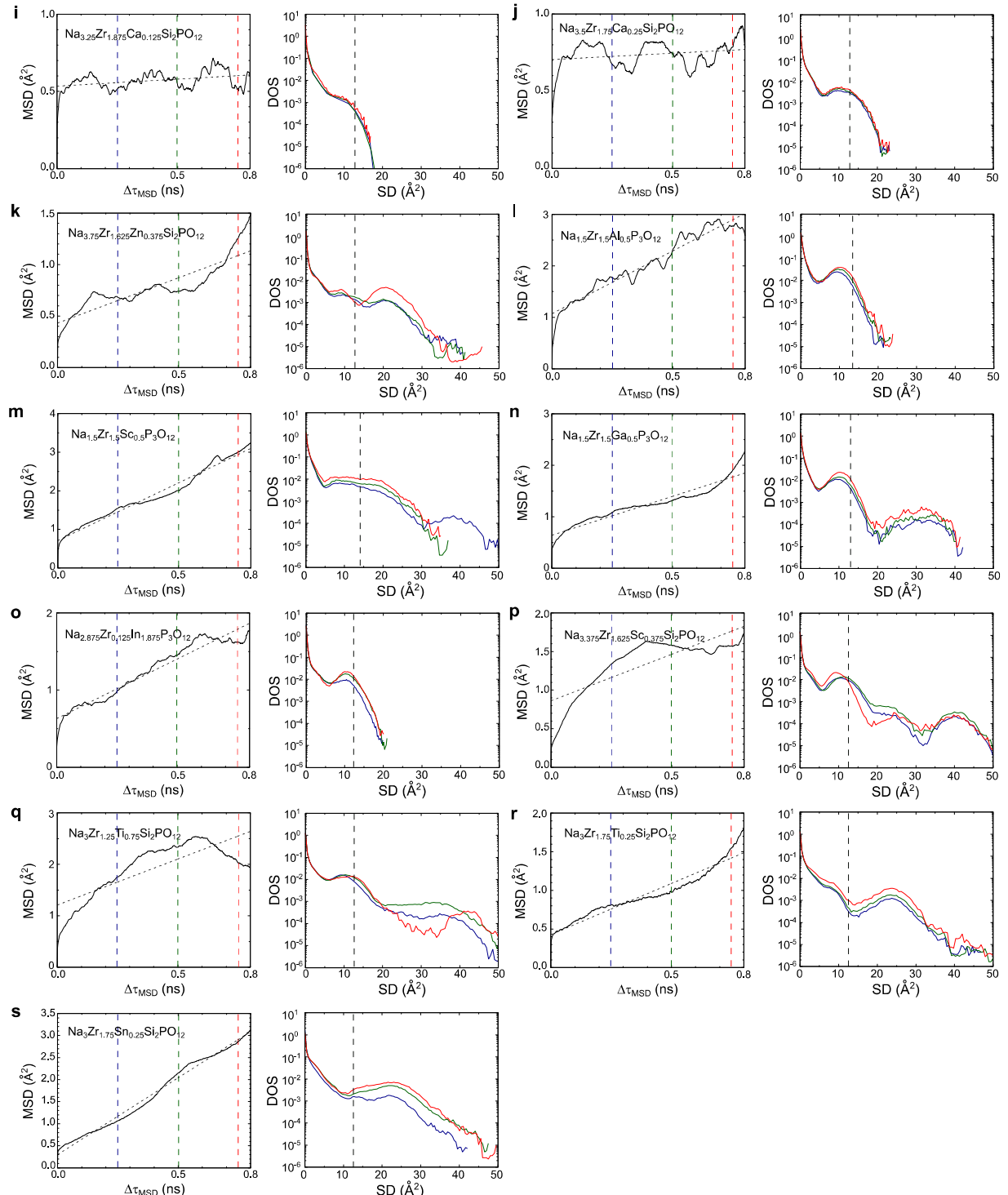
² Research Center for Energy and Environmental Materials (GREEN), National Institute for Materials Science (NIMS), 1-1 Namiki, Tsukuba, Ibaraki 305-0044, Japan

³ Laboratory for Chemistry and Life Science, Tokyo Institute of Technology, 4259 Nagatsuta, Midori-ku, Yokohama, 226-8501, Japan

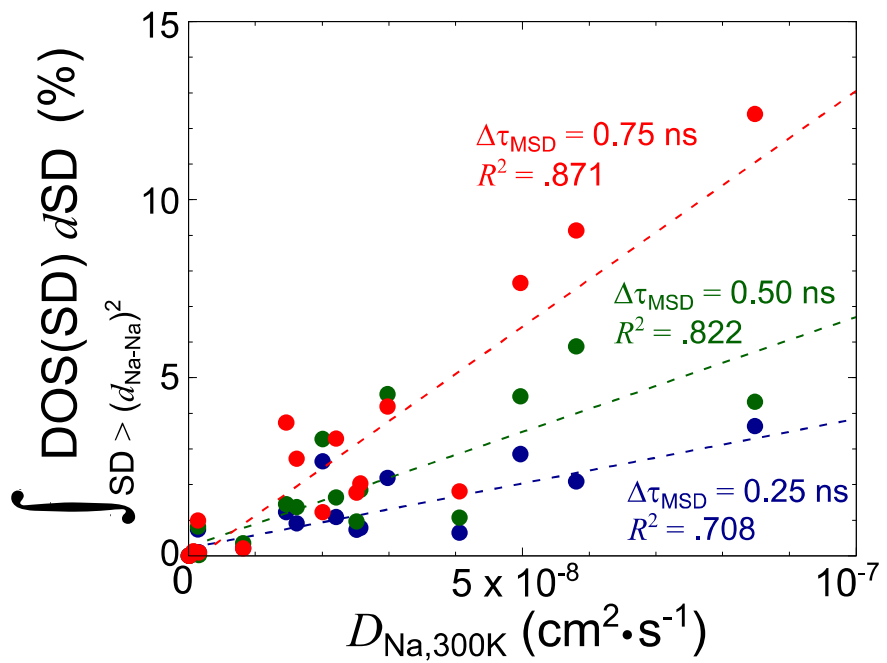
*Corresponding author: jang.seonghoon.b4@tohoku.ac.jp



Supplementary Fig. 1 Mean squared displacement (MSD) curves (left) and the density of states (DOS) for the trajectory samples, that is, squared displacement (SQ) data points across ensembles and times (right). They were given by single- T “long-time” diagnoses (with $\Delta\tau = 1$ fs and $\tau = 1$ ns at $T = 300$ K). In the left plot for each case, the black dashed line represents regressions against sampled time intervals $\Delta\tau_{\text{MSD}}$, and the blue, green, and red vertical dashed lines denote $\Delta\tau_{\text{MSD}} = 0.25, 0.50$, and 0.75 ns, respectively, which correspond to the DOS curves of the same colors in the right plot for each case. The black vertical dashed line in the right plot for each case denotes $\text{SD} = \langle d_{\text{Na-Na}} \rangle^2$, the squared Na-Na bond distance. The area for each DOS plot is normalized to 1. For $\langle d_{\text{Na-Na}} \rangle$, refer to Supplementary Table 2.



(to be continued)

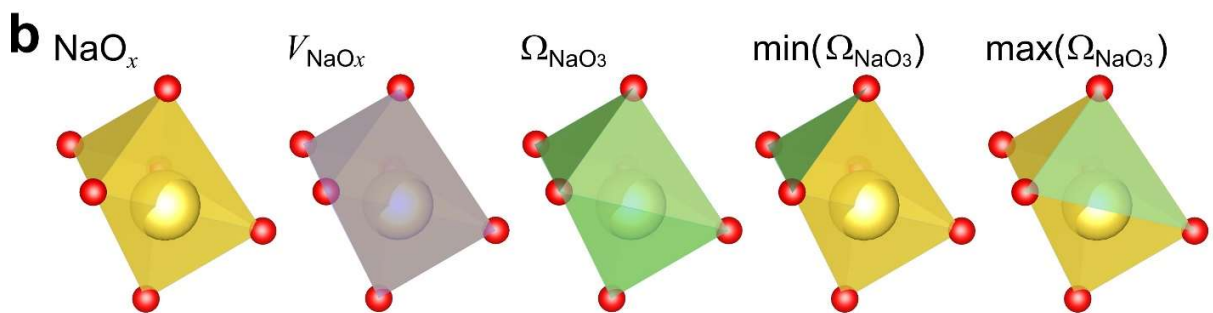
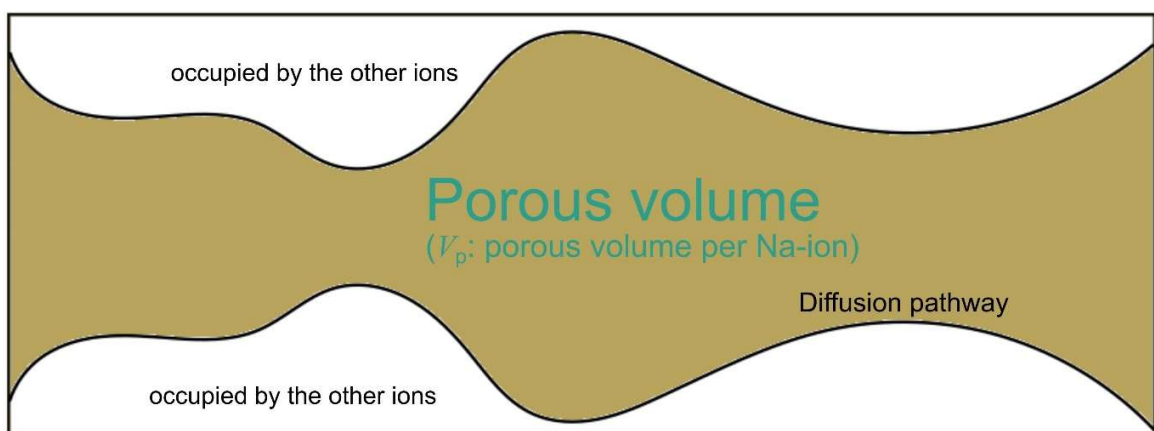
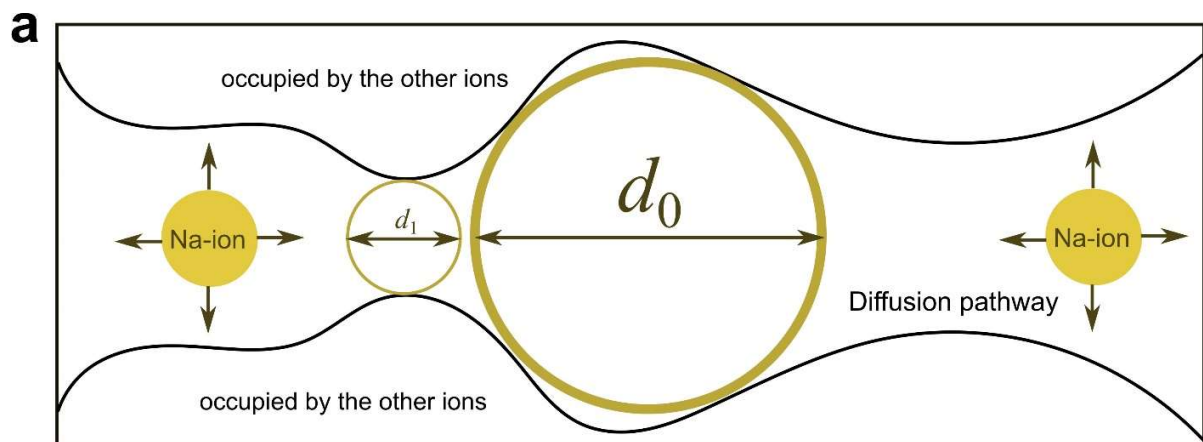


Supplementary Fig. 2 DOS areas with $\text{SD} > \langle d_{\text{Na}-\text{--}} \rangle^2$ are plotted against the room-temperature Na-ion self-diffusion coefficients $D_{\text{Na},300\text{K}}$ calculated from the MSD curves at $\Delta\tau_{\text{MSD}} = 0.25, 0.50$, and 0.75 ns . For $\langle d_{\text{Na}-\text{--}} \rangle$, refer to Supplementary Table 2.

Supplementary Note 1 Considered features (descriptor candidates) for the room-temperature Na-ion self-diffusion coefficients $D_{\text{Na},300\text{K}}$

Supplementary Table 1 Detailed descriptions of considered features (descriptor candidates) for the room-temperature Na-ion self-diffusion coefficient $D_{\text{Na},300\text{K}}$.

Electrostatic feature	
$\langle C_p \rangle$	the average charge for polyhedra MO_y ($M = \text{Ti, Ge, Zr, Mg, Zn, Al, Sc, Ga, In, Si, P, and As}$); the valence (-2) of O were divided by the number of surrounding metal ions since neighboring MO_y are not completely separated.
$\langle \chi_M \rangle$	average of electronegativity χ_M for metal ions (excluding Na-ions)
Diffusion-pathway features	
d_0	the broadest width along the diffusion paths for Na-ions
d_1	the bottleneck width along the diffusion paths for Na-ions
V_p	the porous volume given to a Na-ion
ρ_{Na}	Na-ion density
n	Na-ion content as of $\text{Na}_nM_mM'_{m'}\text{Si}_{3-p-a}\text{P}_p\text{As}_a\text{O}_{12}$
$\langle d_{\text{Na-Na}} \rangle$	the average Na-Na bond length
$\text{med}(d_{\text{Na-Na}})$	the median Na-Na bond length
$\langle r_M \rangle$	the average of ionic radii r_M for metal ions (excluding Na-ions)
Geometrical features	
$\langle d_{\text{Na-O}} \rangle$	the average Na-O bond length
$\langle n_{\text{Na-O}} \rangle$	the average coordination number for a Na-ion to O-ions
Site-specific local geometrical features (especially for polyhedra NaO_x)	
$\langle V_{\text{NaO}_x} \rangle$	the average volume of polyhedra NaS_x
$\langle \min(\Omega_{\text{NaO}_3}) \rangle$	the average narrowest Na-3O solid angle for polyhedra NaO_x
$\langle \Omega_{\text{NaO}_3} \rangle$	the average Na-3O solid angle across for polyhedra NaO_x
$\langle \max(\Omega_{\text{NaO}_3}) \rangle$	the average widest Na-3O solid angle for polyhedra NaO_x
$\text{stdev}(\Omega_{\text{NaO}_3})$	the standard deviation of the Na-3O solid angles for polyhedra NaO_x



Supplementary Fig. 3 Schematic illustrations of **a** diffusion-pathway features d_0 , d_1 , and V_p and **b** site-specific local geometrical features V_{NaO_x} , Ω_{NaO_3} , $\min(\Omega_{\text{NaO}_3})$, and $\max(\Omega_{\text{NaO}_3})$. For the definitions, Supplementary Table 1 is referred to.

The descriptions of the 17 features x_i are provided in Supplementary Table 1. We also illustrate the diffusion-pathway features d_0 , d_1 , and V_p and site-specific local geometrical features V_{NaO_x} , Ω_{NaO_3} , $\min(\Omega_{\text{NaO}_3})$, and $\max(\Omega_{\text{NaO}_3})$ in Supplementary Fig. 3. To obtain the estimates for $x_i = d_0$, d_1 , and V_p , a Voronoi tessellation technique was employed on the given sample cell space after manually excluding Na-ions. By using the Voronoi nodes obtained from the tessellation, d_0 represents the diameter of the largest sphere centered on a node that touches the surface of the remaining ions. It corresponds to the widest section along the diffusion path. Meanwhile, d_1 corresponds to the diameter of the largest sphere that can move along the nodes, representing the narrowest section along the diffusion path. Additionally, V_p refers to the probe-occupiable volume per Na-ion. Since Na-ions were excluded from the sample cell, a probe with the size of a Na-ion ionic radius (1.0 \AA^3)³ can move freely within the void. In the analysis, the Shannon ionic radii for the considered ion sites were referred to,¹ and the Zeo++ package was utilized for the calculations.²

3

Supplementary Table 2 Feature dataset for the 19 samples given in Table 1. The definitions for the descriptors are given in Supplementary Table 1. The average $\langle r_M \rangle$ of ionic radii r_M for metal ions and the volume V for a unit cell of each sample are also presented. In the last column, we added the case of $\text{Na}_{2.75}\text{Zr}_{1.75}\text{Nb}_{0.25}\text{Si}_2\text{PO}_{12}$.

Descriptor	$\text{NaTi}_2\text{P}_3\text{O}_{12}$	$\text{NaGe}_2\text{P}_3\text{O}_{12}$	$\text{NaZr}_2\text{P}_3\text{O}_{12}$	$\text{NaZr}_2\text{As}_3\text{O}_{12}$
$\langle C_P \rangle$	-0.184	-0.184	-0.184	-0.184
$\langle \chi_M \rangle$	1.93	2.12	1.85	1.84
d_0 (Å)	2.38	2.33	2.60	2.51
d_1 (Å)	1.57	1.37	1.73	1.75
V_p (Å ³)	3.00	2.46	20.6	40.0
ρ_{Na} (Å ⁻³)	0.00421	0.00462	0.00378	0.00340
n	1	1	1	1
$\langle d_{\text{Na}-\text{Na}} \rangle$ (Å)	3.78	3.73	4.06	4.03
med($d_{\text{Na}-\text{Na}}$) (Å)	3.78	3.73	4.06	4.03
$\langle d_{\text{Na}-\text{O}} \rangle$ (Å)	2.49	2.47	2.57	2.55
$\langle n_{\text{Na}-\text{O}} \rangle$	5.07	5.17	4.93	4.74
$\langle V_{\text{NaO}_x} \rangle$ (Å ³)	16.7	16.5	17.7	17.2
$\langle \min(\Omega_{\text{NaO}_3}) \rangle$	0.631	0.569	0.656	0.655
$\langle \Omega_{\text{NaO}_3} \rangle$	1.48	1.40	1.57	1.57
$\langle \max(\Omega_{\text{NaO}_3}) \rangle$	2.15	2.41	2.09	2.08
stdev(Ω_{NaO_3})	0.592	0.691	0.568	0.573
$\langle r_M \rangle$ (Å)	0.344	0.314	0.390	0.489
V (Å ³)	1900	1730	2120	2350

(to be continued)

Descriptor	Na ₃ In ₂ P ₃ O ₁₂	Na ₃ Zr ₂ Si ₂ PO ₁₂	Na _{3.25} Zr _{1.875} Mg _{0.125} Si ₂ PO ₁₂	Na _{3.75} Zr _{1.625} Mg _{0.375} Si ₂ PO ₁₂
$\langle C_P \rangle$	-0.579	-0.622	-0.583	-0.694
$\langle \chi_M \rangle$	2.03	1.73	1.73	1.73
d_0 (Å)	2.47	2.54	2.53	2.54
d_1 (Å)	1.65	1.72	1.67	1.63
V_p (Å ³)	9.02	10.1	9.28	7.40
ρ_{Na} (Å ⁻³)	0.0112	0.0109	0.0118	0.0137
n	3	3	3.25	3.75
$\langle d_{\text{Na-Na}} \rangle$ (Å)	3.47	3.57	3.59	3.55
med($d_{\text{Na-Na}}$) (Å)	3.47	3.51	3.57	3.51
$\langle d_{\text{Na-O}} \rangle$ (Å)	2.56	2.58	2.57	2.57
$\langle n_{\text{Na-O}} \rangle$	5.64	5.58	5.34	5.10
$\langle V_{\text{NaO}_x} \rangle$ (Å ³)	20.9	18.8	17.1	16.3
$\langle \min(\Omega_{\text{NaO}_3}) \rangle$	0.714	0.604	0.605	0.551
$\langle \Omega_{\text{NaO}_3} \rangle$	1.35	1.40	1.50	1.53
$\langle \max(\Omega_{\text{NaO}_3}) \rangle$	2.72	2.71	3.25	3.43
stdev(Ω_{NaO_3})	0.647	0.806	0.926	0.972
$\langle r_M \rangle$ (Å)	0.422	0.426	0.426	0.426
V (Å ³)	2150	2200	2200	2200

(to be continued)

Descriptor	$\text{Na}_{3.25}\text{Zr}_{1.875}\text{Ca}_{0.125}\text{Si}_2\text{PO}_{12}$	$\text{Na}_{3.5}\text{Zr}_{1.75}\text{Ca}_{0.25}\text{Si}_2\text{PO}_{12}$	$\text{Na}_{3.75}\text{Zr}_{1.625}\text{Zn}_{0.375}\text{Si}_2\text{PO}_{12}$	$\text{Na}_{1.5}\text{Zr}_{1.5}\text{Al}_{0.5}\text{P}_3\text{O}_{12}$
$\langle C_p \rangle$	-0.583	-0.639	-0.722	-0.216
$\langle \chi_M \rangle$	1.72	1.71	1.75	1.71
d_0 (Å)	2.58	2.57	2.56	2.59
d_1 (Å)	1.64	1.65	1.63	1.76
V_p (Å ³)	9.53	8.67	7.51	9.99
ρ_{Na} (Å ⁻³)	0.0118	0.0126	0.0136	0.00587
n	3.25	3.5	3.75	1.5
$\langle d_{\text{Na}-\text{Na}} \rangle$ (Å)	3.59	3.57	3.55	3.66
med($d_{\text{Na}-\text{Na}}$) (Å)	3.57	3.59	3.49	3.61
$\langle d_{\text{Na}-\text{O}} \rangle$ (Å)	2.58	2.60	2.57	2.54
$\langle n_{\text{Na}-\text{O}} \rangle$	5.48	5.45	5.25	5.29
$\langle V_{\text{NaO}_x} \rangle$ (Å ³)	18.1	18.3	16.5	17.3
$\langle \min(\Omega_{\text{NaO}_3}) \rangle$	0.638	0.562	0.582	0.626
$\langle \Omega_{\text{NaO}_3} \rangle$	1.47	1.47	1.53	1.45
$\langle \max(\Omega_{\text{NaO}_3}) \rangle$	3.07	3.42	3.37	2.50
stddev(Ω_{NaO_3})	0.884	0.978	0.949	0.712
$\langle r_M \rangle$ (Å)	0.433	0.440	0.428	0.318
V (Å ³)	2210	2230	2200	2050

(to be continued)

Descriptor	$\text{Na}_{1.5}\text{Zr}_{1.5}\text{Sc}_{0.5}\text{P}_3\text{O}_{12}$	$\text{Na}_{1.5}\text{Zr}_{1.5}\text{Ga}_{0.5}\text{P}_3\text{O}_{12}$	$\text{Na}_{2.875}\text{Zr}_{0.125}\text{In}_{1.875}\text{P}_3\text{O}_{12}$	$\text{Na}_{3.375}\text{Zr}_{1.625}\text{Sc}_{0.375}\text{Si}_2\text{PO}_{12}$
$\langle C_P \rangle$	-0.216	-0.216	-0.514	-0.639
$\langle \chi_M \rangle$	1.85	1.89	2.01	1.73
d_0 (Å)	2.69	2.59	2.58	2.55
d_1 (Å)	1.77	1.73	1.62	1.62
V_p (Å ³)	15.5	10.1	9.31	9.28
ρ_{Na} (Å ⁻³)	0.00564	0.00579	0.0107	0.0123
n	1.5	1.5	2.875	3.375
$\langle d_{\text{Na}-\text{Na}} \rangle$ (Å)	3.77	3.62	3.52	3.54
med($d_{\text{Na}-\text{Na}}$) (Å)	3.81	3.62	3.50	3.53
$\langle d_{\text{Na}-\text{O}} \rangle$ (Å)	2.55	2.55	2.54	2.57
$\langle n_{\text{Na}-\text{O}} \rangle$	4.95	5.40	5.39	5.21
$\langle V_{\text{NaO}_x} \rangle$ (Å ³)	16.4	17.7	18.4	17.8
$\langle \min(\Omega_{\text{NaO}_3}) \rangle$	0.568	0.605	0.787	0.667
$\langle \Omega_{\text{NaO}_3} \rangle$	1.54	1.44	1.45	1.49
$\langle \max(\Omega_{\text{NaO}_3}) \rangle$	2.74	2.70	2.87	3.19
stdev(Ω_{NaO_3})	0.730	0.778	0.767	0.884
$\langle r_M \rangle$ (Å)	0.393	0.380	0.420	0.428
V (Å ³)	2130	2070	2140	2200

(to be continued)

Descriptor	$\text{Na}_3\text{Zr}_{1.25}\text{Ti}_{0.75}\text{Si}_2\text{PO}_{12}$	$\text{Na}_3\text{Zr}_{1.75}\text{Ti}_{0.25}\text{Si}_2\text{PO}_{12}$	$\text{Na}_3\text{Zr}_{1.75}\text{Sn}_{0.25}\text{Si}_2\text{PO}_{12}$	Mean	Standard deviation
$\langle C_p \rangle$	-0.583	-0.583	-0.583	-0.458	0.209
$\langle \chi_M \rangle$	1.76	1.74	1.76	1.82	0.123
d_0 (Å)	2.44	2.49	2.49	2.53	0.0824
d_1 (Å)	1.67	1.63	1.67	1.66	0.0882
V_p (Å ³)	7.54	9.61	9.93	11.0	8.00
ρ_{Na} (Å ⁻³)	0.0112	0.0111	0.0110	0.00922	0.00364
n	3	3	3	2.49	1.04
$\langle d_{\text{Na}-\text{Na}} \rangle$ (Å)	3.57	3.54	3.55	3.64	0.164
med($d_{\text{Na}-\text{Na}}$) (Å)	3.52	3.52	3.53	3.63	0.175
$\langle d_{\text{Na}-\text{O}} \rangle$ (Å)	2.56	2.57	2.57	2.56	0.0312
$\langle n_{\text{Na}-\text{O}} \rangle$	5.39	5.57	5.52	5.29	0.245
$\langle V_{\text{NaO}_x} \rangle$ (Å ³)	18.1	19.1	18.4	17.8	1.13
$\langle \min(\Omega_{\text{NaO}_3}) \rangle$	0.619	0.658	0.611	1.42	2.86
$\langle \Omega_{\text{NaO}_3} \rangle$	1.43	1.40	1.42	1.47	0.0629
$\langle \max(\Omega_{\text{NaO}_3}) \rangle$	2.99	2.79	2.86	2.81	0.428
stdev(Ω_{NaO_3})	0.840	0.783	0.860	0.786	0.132
$\langle r_M \rangle$ (Å)	0.409	0.420	0.425	0.407	0.0429
V (Å ³)	2130	2170	2190	2140	133

(to be continued)

Descriptor	$\text{Na}_{2.75}\text{Zr}_{1.75}\text{Nb}_{0.25}\text{Si}_2\text{PO}_{12}$
$\langle C_p \rangle$	-0.556
$\langle \chi_M \rangle$	1.74
d_0 (Å)	2.54
d_1 (Å)	1.70
V_p (Å ³)	10.3
ρ_{Na} (Å ⁻³)	0.0101
n	2.75
$\langle d_{\text{Na-Na}} \rangle$ (Å)	3.56
med($d_{\text{Na-Na}}$) (Å)	3.54
$\langle d_{\text{Na-O}} \rangle$ (Å)	2.57
$\langle n_{\text{Na-O}} \rangle$	5.30
$\langle V_{\text{NaO}_x} \rangle$ (Å ³)	17.8
$\langle \min(\Omega_{\text{NaO}_3}) \rangle$	0.678
$\langle \Omega_{\text{NaO}_3} \rangle$	1.49
$\langle \max(\Omega_{\text{NaO}_3}) \rangle$	3.08
stdev(Ω_{NaO_3})	0.830
$\langle r_M \rangle$ (Å)	0.422
V (Å ³)	2180

Supplementary Note 2 Maximum likelihood estimation and pseudo-goodness-of-fit R^2_{pseudo} for the exhaustive search of the possible multivariate beta regression models

In beta regression modelling, it is assumed that each η_j (score of $D_{\text{Na},300\text{K}}$ for datum $j: j = 1, \dots, n_{\text{data}}$) follows the beta distribution: $\eta_j \sim \text{B}(\eta_j; \bar{\eta}_j, \varphi)$:

$$\text{B}(\eta_j; \bar{\eta}_j, \varphi) = \frac{\int_0^\infty t^{\varphi-1} e^{-t} dt}{\int_0^\infty t^{\bar{\eta}_j \varphi - 1} e^{-t} dt \int_0^\infty t^{[(1-\bar{\eta}_j)\varphi]-1} e^{-t} dt} \eta_j^{\bar{\eta}_j \varphi - 1} (1 - \eta_j)^{(1-\bar{\eta}_j)\varphi - 1}, \quad (\text{S1})$$

where $\bar{\eta}_j$ and φ denote the most-fit value $\bar{\eta}$ for η_j (given as the mean for B) and the common precision for B, respectively.^{4, 5} Then, by executing maximum likelihood estimation with parameters $c(x_i)$, c , and φ towards the minimization of the sum \mathcal{L} of the logarithm-scaled beta densities (i.e., the log-likelihood function proposed by Ferrari and Cribari-Neto)⁵ given by

$$\mathcal{L} = \sum_{j=1}^{n_{\text{data}}} \log_e [\text{B}(\eta_j; \bar{\eta}_j, \varphi)], \quad (\text{S2})$$

the most-fitting h (consequently, $\bar{\eta}$) would be found from the input η and $z[x_i]$.

We set $df = 1$ and 2, with which we exhaustively examined 153 [= $\sum_{df=1,2} \binom{n(x_i)}{df}$]; see the number $n(x_i)$ of features (descriptor candidates) x_i is 17] multivariate regression models and picked the two models with the highest pseudo-goodness-of-fit values R^2_{pseudo} .⁵

$$R^2_{\text{pseudo}} = R^2[h(\bar{\eta}_j), h(\eta_j)], \quad (\text{S3})$$

that is, the R^2 value between $h(\bar{\eta}_j)$ and $h(\eta_j)$: $h(\bar{\eta}_j) = \log_e \frac{\bar{\eta}_j}{1-\bar{\eta}_j}$ and $h(\eta_j) = \log_e \frac{\eta_j}{1-\eta_j}$, which is the inverse function of Eq. (11) (i.e., the logit function). In addition to R^2_{pseudo} , we added criteria

that p -values for $c(x_i)$, c , and φ should be less than .05. Also, to examine any multicollinearity issue between x_i , we also computed the Pearson correlation coefficient between the two taken descriptors and x_1 and x_2 :

$$r(x_1, x_2) = \frac{\sum_{j=1}^{n_{\text{data}}}(x_1 - \bar{x}_1)(x_2 - \bar{x}_2)}{\sqrt{\sum_{j=1}^{n_{\text{data}}}(x_1 - \bar{x}_1)^2} \sqrt{\sum_{j=1}^{n_{\text{data}}}(x_2 - \bar{x}_2)^2}}, \quad (\text{S4})$$

where \bar{x}_i is the mean value of x_1 .

Supplementary Note 3 Descriptors for $D_{\text{Na},300\text{K}}$ in NASICONs and Na-ion sulfides

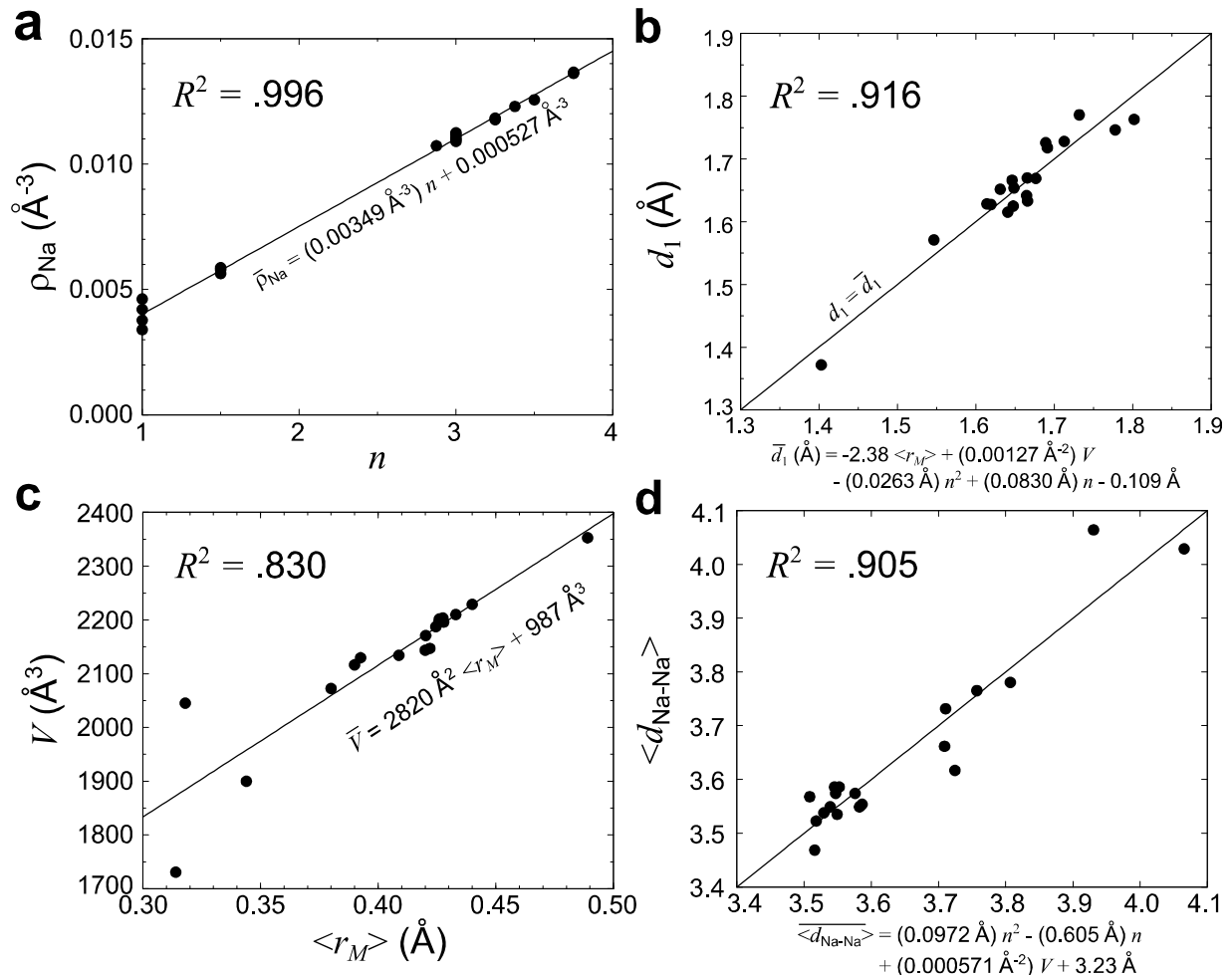
In our previous study on Na-ion sulfides, where tetrahedral units MS_4 are separated, we conducted a statistical analysis and found that structural distortions in NaS_x , specifically towards wide faces [indicated by large $\langle \max(\Omega_{\text{NaS}_3}) \rangle$], along with shallow electrostatic potential (by small $\langle C_p \rangle$), play a crucial role in increasing $D_{\text{Na},300\text{K}}$.⁶ We further confirmed the positive influence of such structural distortions on $D_{\text{Na},300\text{K}}$ in NASICON samples through another beta regression model. The multivariate beta regression model with the highest R^2_{pseudo} given two descriptors allowed [one of which was set to $\langle \max(\Omega_{\text{NaO}_3}) \rangle$] was identified as

$$h = 0.631 z[\langle V_{\text{NaO}_x} \rangle] + 0.585 z[\langle \max(\Omega_{\text{NaO}_3}) \rangle] + 0.488 \quad (\text{S5})$$

with $\varphi = 3.23 : R^2_{\text{pseudo}} = .454$. The Pearson correlation coefficient between $\langle V_{\text{NaO}_x} \rangle$ and $\langle \max(\Omega_{\text{NaO}_3}) \rangle$ was given as $r(\langle V_{\text{NaO}_x} \rangle, \langle V_{\text{NaO}_x} \rangle) = .00402$, indicating the absence of the significant multicollinearity issue within Eq. (S5). Given the higher R^2_{pseudo} value for Eq. (2), namely $R^2_{\text{pseudo}} = 0.797$, compared to Eq. (S5), it is suggested that modulating d_1 and $\langle d_{\text{Na-Na}} \rangle$, rather than $\langle \max(\Omega_{\text{NaO}_3}) \rangle$, is more favorable to achieve higher $D_{\text{Na},300\text{K}}$ for NASICONs. This implies that, in the case of NASICON structures, enhancing the already-established diffusion pathways indicated by the underlying “skeleton” structure (represented by d_1) and optimizing the proximity of Na-ions along these pathways ($\langle d_{\text{Na-Na}} \rangle$) are advantageous. It is suggested that the focus should not solely be on designing local structures associated with polyhedra NaO_x , but rather on manipulating the overall framework to facilitate efficient ion mobility, especially for NASICONs. Meanwhile, it is worth noting that NASICONs taking high-valence ions, such as As

or P, already exhibit small $\langle C_P \rangle$ values within the range of [-0.722, -0.184], whereas Na-ion sulfides display larger and more widely distributed $\langle C_P \rangle$ values within the range of [-6, -2.5].⁶

Supplementary Note 4 Linear regressions for the primary descriptors against the secondary ones



Supplementary Fig. 4 Linear regression models for ρ_{Na} , d_1 , V , and $\langle d_{\text{Na}-\text{N}} \rangle$ given in Eqs. (S6)–(S9). The dots are estimated from the unit cell samples of which geometry was optimized by density functional theory (DFT) calculations, and the lines show the regressed (simulated) results.

Our goal is to develop models wherein the Na-ion density ρ_{Na} , the bottleneck width d_1 , and the average Na-Na bond length $\langle d_{\text{Na}-\text{Na}} \rangle$ eventually are connected to the Na-ion content n and the average $\langle r_M \rangle$ of ionic radii r_M for metal ions (excluding Na-ions),³ with $R^2 > 0.9$ if attainable, to keep the internal consistency of the whole modelling. We briefly note that the potential multicollinearity problem is not of significant concern, as far as these equations play a crucial role in predicting $\sigma_{\text{Na},300\text{K}}$ eventually. The results were given below;

$$\rho_{\text{Na}} = (0.00349 \text{ \AA}^{-3})n + 0.000527 \text{ \AA}^{-3}, \quad (\text{S6})$$

$$d_1 = -2.38 \langle r_M \rangle + (0.00127 \text{ \AA}^{-2})V - (0.0263 \text{ \AA})n^2 + (0.0830 \text{ \AA})n - 0.109 \text{ \AA}, \quad (\text{S7})$$

$$V = (2820 \text{ \AA}^2) \langle r_M \rangle + 987 \text{ \AA}^3, \quad (\text{S8})$$

and

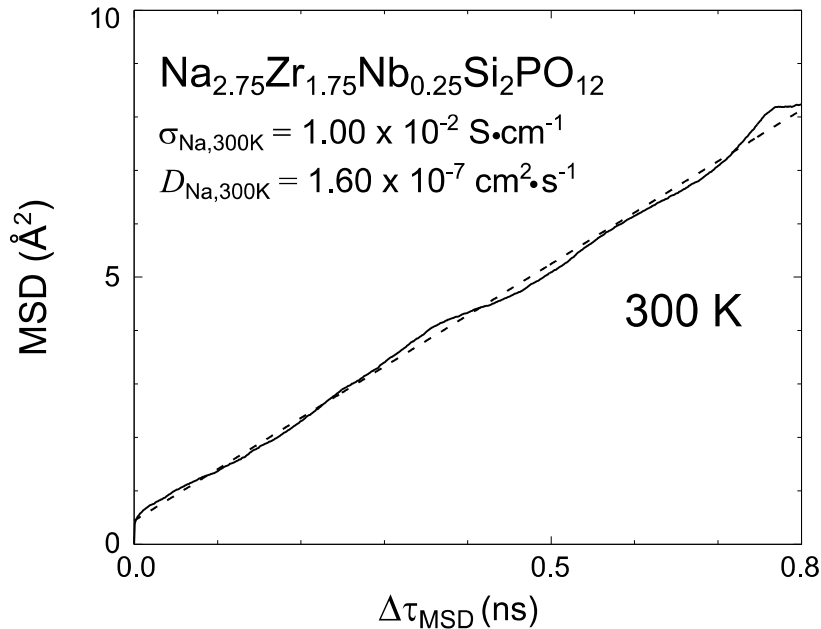
$$\langle d_{\text{Na}-\text{Na}} \rangle = (0.0972 \text{ \AA})n^2 - (0.605 \text{ \AA})n + (0.000571 \text{ \AA}^{-2})V + 3.23 \text{ \AA}, \quad (\text{S9})$$

where V denotes the volume for a unit cell of each sample. ρ_{Na} will increase with n . R^2 for Eqs. (S6)–(S9) were given as 0.996, 0.916, 0.830, and 0.905, respectively. In Supplementary Fig. 4a and Eq. (S6), n suffices the regression modelling for ρ_{Na} without V . In Supplementary Fig. 4c and Eq. (S8), R^2 rises to 0.943 subsequent to the removal of an outlier, the case of $\text{Na}_{1.5}\text{Zr}_{1.5}\text{Al}_{0.5}\text{P}_3\text{O}_{12}$ characterized by the compressed $V = 1880 \text{ \AA}^3$. It is noteworthy that, $R^2 > 0.9$ for V necessitated the incorporation of interactive terms $(n(r_M))^k$ with $k = 1$ and 2.

d_1 would be maximized by taking a small $\langle r_M \rangle$ in V (expanded by, on the contrary, large $\langle r_M \rangle$) and optimizing the Na-ion content n around 1.58. $\langle d_{\text{Na}-\text{Na}} \rangle$ would be minimized by taking a small V and optimizing n around 3.11. Hence, the optimizing values n for d_1 and $\langle d_{\text{Na}-\text{Na}} \rangle$ are

opposite, and other related factors such as $\langle r_M \rangle$ and V (that is regressed against $\langle r_M \rangle$ again) should be considered as well to model the room-temperature Na-ion conductivity $\sigma_{\text{Na},300\text{K}}$ correctly.

Supplementary Note 5 Single-*T* “long-time” diagnosis for $\text{Na}_{2.75}\text{Zr}_{1.75}\text{Nb}_{0.25}\text{Si}_2\text{PO}_{12}$



Supplementary Fig. 5 Mean squared displacement curve against sampled time intervals $\Delta\tau_{\text{MSD}}$ given by the single-*T* “long-time” diagnosis (with $\Delta\tau = 1$ fs and $\tau = 1$ ns at $T = 300$ K) for $\text{Na}_{2.75}\text{Zr}_{1.75}\text{Nb}_{0.25}\text{Si}_2\text{PO}_{12}$. The black dashed line represents regression against sampled time intervals $\Delta\tau_{\text{MSD}}$.

We conducted the single-*T* “long-time” diagnosis for $\text{Na}_{2.75}\text{Zr}_{1.75}\text{Nb}_{0.25}\text{Si}_2\text{PO}_{12}$. The obtained results were highly remarkable in an unexpected way, as evidenced by $\sigma_{\text{Na},300\text{K}} = 1.00 \times 10^{-2} \text{ S}\cdot\text{cm}^{-1}$ and $D_{\text{Na},300\text{K}} = 1.60 \times 10^{-7} \text{ cm}^2\cdot\text{s}^{-1}$. In Supplementary Fig. 5, we depict the nearly linear MSD curves $R_{\text{MSD}}^2 = 0.997$. We postulate that the disparities observed in the values of $\sigma_{\text{Na},300\text{K}}$ between the two approaches (that is, the single-*T* “long-time” diagnosis and the multi-

T DFT-MD simulations) can be attributed to a technical issue, specifically, the contraction of unit cell volumes V during the NpT pre-treatment stage for the latter: 4.66 %. While V was fixed to the geometry-optimized one in the single- T “long-time” diagnosis, the multi- T DFT-MD simulations employed the unit cell whose V was thermally equilibrated during the NpT pre-treatment to include the high- T effect for E_a more accurately. On the contrary, the different choice of k -grids and the kinetic energy cutoff between the geometry optimization and the NpT pre-treatment at low T may have elicited the V contraction and sensitive steric hindrance effects for the self-diffusion of Na-ions. Given the prevalent overestimation problem associated with lattice constants in the generalized gradient approximation scheme,^{7, 8} the true $\sigma_{\text{Na},300\text{K}}$ likely resides between the two $\sigma_{\text{Na},300\text{K}}$ (that is, still in the order of 10^{-3} S·cm⁻¹), which may be addressed in future study with experimental supports. Nonetheless, in both approaches, our findings assert that the structurally-stable $\text{Na}_{2.75}\text{Zr}_{1.75}\text{Nb}_{0.25}\text{Si}_2\text{PO}_{12}$, which hitherto remain unexplored and validate the predictability of our model $\sigma_{\text{Na},300\text{K},\text{sim}}$, hold substantial promise for future investigation.

Supplementary Table 3 Values for n , $\langle r_M \rangle$, and the experimental values for $\sigma_{Na,300K}$, which were referred to by Eqs. (7) and (8). $\sigma_{Na,300K}$ were interpolated or measured at $T = 300$ K⁹⁻¹⁹ or extrapolated to $T = 300$ K.²⁰⁻³⁴

Chemical formula								n	$\langle r_M \rangle$	experimental $\sigma_{Na,300K}$ (S·cm ⁻¹)
Na 1	Zr 2	Y 1		P 3		O 12	1	0.475	1.60×10^{-79}	
Na 1.5	Zr 1.5	Y 0.5		P 3		O 12	1.5	0.408	2.73×10^{-69}	
Na 2	Zr 1	Y 1		P 3		O 12	2	0.426	8.55×10^{-69}	
Na 2.5	Zr 0.5	Y 1.5		P 3		O 12	2.5	0.444	9.09×10^{-79}	
Na 3	Zr 2			Si 2	P 1	O 12	3	0.426	4.00×10^{-310}	
Na 3.1	Zr 1.55			Si 2.3	P 0.7	O 11	3.1	0.403	5.00×10^{-410}	
Na 3.1	Zr 2	Al 0.1		Si 1.9	P 1	O 12	3.1	0.432	2.00×10^{-410}	
Na 3.2	Zr 2	Al 0.2		Si 1.8	P 1	O 12	3.2	0.437	2.00×10^{-410}	
Na 3.3	Zr 1.55	Al 0.2		Si 2.1	P 0.7	O 11	3.3	0.415	4.00×10^{-410}	
Na 3.4	Zr 1.55	Al 0.3		Si 2	P 0.7	O 11	3.4	0.421	1.00×10^{-410}	
Na 2.4		Hf 2		Si 1.4	P 1.6	O 12	2.4	0.411	7.30×10^{-411}	
Na 2.6		Hf 2		Si 1.6	P 1.4	O 12	2.6	0.415	5.90×10^{-411}	
Na 2.8		Hf 2		Si 1.8	P 1.2	O 12	2.8	0.418	6.90×10^{-411}	
Na 3		Hf 2		Si 2	P 1	O 12	3	0.422	1.10×10^{-311}	
Na 3.2		Hf 2		Si 2.2	P 0.8	O 12	3.2	0.426	2.30×10^{-311}	
Na 3.4		Hf 2		Si 2.4	P 0.6	O 12	3.4	0.429	1.40×10^{-311}	
Na 3.6		Hf 2		Si 2.6	P 0.4	O 12	3.6	0.433	1.20×10^{-311}	
Na 3.8		Hf 2		Si 2.8	P 0.2	O 12	3.8	0.436	3.20×10^{-411}	
Na 3	Zr 1.88	Si 2	Y 0.12	P 1		O 11.94	3	0.430	2.50×10^{-312}	
Na 3.4		Sc 2		Si 0.4	P 2.6	O 12	3.4	0.407	6.90×10^{-413}	
Na 3.1	Zr 1.95	Mg 0.05		Si 2	P 1	O 12	3.1	0.426	3.50×10^{-314}	
Na 3	Zr 2			Si 2	P 1	O 12	3	0.426	1.10×10^{-415}	
Na 3	Zr 1.9	Yb 0.1		Si 2	P 1	O 12	3	0.429	1.70×10^{-415}	
Na 3	Zr 1.9	Gd 0.1		Si 2	P 1	O 12	3	0.430	6.00×10^{-415}	
Na 3	Zr 1.9	Ce 0.1		Si 2	P 1	O 12	3	0.429	9.00×10^{-415}	
Na 3	Zr 2			Si 2	P 1	O 12	3	0.426	2.00×10^{-316}	
Na 3.2	Zr 1.8	Sc 0.2		Si 2	P 1	O 12	3.2	0.427	5.30×10^{-316}	
Na 3.4	Zr 1.6	Sc 0.4		Si 2	P 1	O 12	3.4	0.428	6.20×10^{-316}	
Na 3.6	Zr 1.4	Sc 0.6		Si 2	P 1	O 12	3.6	0.429	5.10×10^{-316}	

Na	3	Zr	2		Si	2	P	1	O	12	3	0.426	3.80×10^{-4} ¹⁷	
Na	3.1	Zr	1.95	Ca	0.05	Si	2	P	1	O	12	3.1	0.429	7.58×10^{-4} ¹⁷
Na	3.2	Zr	1.9	Ca	0.1	Si	2	P	1	O	12	3.2	0.432	1.67×10^{-3} ¹⁷
Na	3.3	Zr	1.85	Ca	0.15	Si	2	P	1	O	12	3.3	0.434	1.33×10^{-3} ¹⁷
Na	3.4	Zr	1.8	Ca	0.2	Si	2	P	1	O	12	3.4	0.437	6.41×10^{-4} ¹⁷
Na	3.5	Zr	1.75	Ca	0.25	Si	2	P	1	O	12	3.5	0.440	9.95×10^{-4} ¹⁷
Na	3.3	Zr	2		Si	2.3	P	0.7	O	12	3.3	0.431	2.14×10^{-3} ¹⁸	
Na	3.35	Zr	1.95	Nb	0.05	Si	2.4	P	0.6	O	12	3.35	0.432	4.06×10^{-3} ¹⁸
Na	3.3	Zr	1.9	Nb	0.1	Si	2.4	P	0.6	O	12	3.3	0.432	5.51×10^{-3} ¹⁸
Na	3.25	Zr	1.85	Nb	0.15	Si	2.4	P	0.6	O	12	3.25	0.431	4.44×10^{-3} ¹⁸
Na	3.2	Zr	1.8	Nb	0.2	Si	2.4	P	0.6	O	12	3.2	0.430	2.94×10^{-3} ¹⁸
Na	3.1	Zr	1.7	Nb	0.3	Si	2.4	P	0.6	O	12	3.1	0.428	2.69×10^{-3} ¹⁸
Na	3	Zr	1.6	Nb	0.4	Si	2.4	P	0.6	O	12	3	0.427	1.39×10^{-3} ¹⁸
Na	3.36	Zr	1.96	Nb	0.04	Si	2.4	P	0.6	O	12	3.36	0.433	1.61×10^{-3} ¹⁹
Na	2.96	Zr	1.96	Nb	0.04	Si	2	P	1	O	12	2.96	0.425	4.15×10^{-4} ¹⁹
Na	3.4	Zr	2		Si	2.4	P	0.6	O	12	3.4	0.433	3.65×10^{-4} ¹⁹	
Na	3	Zr	2		Si	2	P	1	O	12	3	0.426	4.21×10^{-4} ¹⁹	
Na	3.08	Zr	1.96	Mg	0.04	Si	2	P	1	O	12	3.08	0.426	1.10×10^{-3} ²⁰
Na	3.2	Zr	1.9	Mg	0.1	Si	2	P	1	O	12	3.2	0.426	4.97×10^{-4} ²⁰
Na	3.6	Zr	1.7	Mg	0.3	Si	2	P	1	O	12	3.6	0.426	4.91×10^{-5} ²⁰
Na	3.08	Zr	1.96	Zn	0.04	Si	2	P	1	O	12	3.08	0.426	4.79×10^{-5} ²⁰
Na	3.2	Zr	1.9	Zn	0.1	Si	2	P	1	O	12	3.2	0.426	1.97×10^{-4} ²⁰
Na	3.4	Zr	1.8	Zn	0.2	Si	2	P	1	O	12	3.4	0.427	5.81×10^{-4} ²⁰
Na	3.6	Zr	1.7	Zn	0.3	Si	2	P	1	O	12	3.6	0.427	3.14×10^{-5} ²⁰
Na	3.04	Zr	1.96	Y	0.04	Si	2	P	1	O	12	3.04	0.427	3.54×10^{-4} ²⁰
Na	3.1	Zr	1.9	Y	0.1	Si	2	P	1	O	12	3.1	0.430	2.08×10^{-3} ²⁰
Na	3.3	Zr	1.7	Y	0.3	Si	2	P	1	O	12	3.3	0.437	1.16×10^{-4} ²⁰
Na	3	Zr	1.9	Ti	0.1	Si	2	P	1	O	12	3	0.424	6.67×10^{-5} ²⁰
Na	3	Zr	1.8	Ti	0.2	Si	2	P	1	O	12	3	0.421	1.25×10^{-4} ²⁰
Na	3	Zr	1.7	Ti	0.3	Si	2	P	1	O	12	3	0.419	9.68×10^{-5} ²⁰
Na	2.96	Zr	1.96	Nb	0.04	Si	2	P	1	O	12	2.96	0.425	3.08×10^{-3} ²⁰
Na	2.9	Zr	1.9	Nb	0.1	Si	2	P	1	O	12	2.9	0.424	5.31×10^{-4} ²⁰
Na	2.96	Zr	1.96	Ta	0.04	Si	2	P	1	O	12	2.96	0.425	1.97×10^{-3} ²⁰
Na	2.9	Zr	1.9	Ta	0.1	Si	2	P	1	O	12	2.9	0.424	6.29×10^{-4} ²⁰
Na	2.96	Zr	1.96	V	0.04	Si	2	P	1	O	12	2.96	0.425	2.34×10^{-3} ²⁰

Na	2.9	Zr	1.9	V	0.1		Si	2	P	1		O	12	2.9	0.422	7.62×10^{-420}	
Na	1	Zr	2					P	3			O	12	1	0.390	4.61×10^{-921}	
Na	1.5	Zr	1.5	In	0.5			P	3			O	12	1.5	0.398	1.29×10^{-721}	
Na	1.8	Zr	1.2	In	0.8			P	3			O	12	1.8	0.403	3.13×10^{-721}	
Na	2	Zr	1	In	1			P	3			O	12	2	0.406	6.60×10^{-721}	
Na	2.2	Zr	0.8	In	1.2			P	3			O	12	2.2	0.409	1.87×10^{-621}	
Na	2.5	Zr	0.5	In	1.5			P	3			O	12	2.5	0.414	1.77×10^{-621}	
Na	2.75	Zr	0.25	In	1.75			P	3			O	12	2.75	0.418	2.42×10^{-621}	
Na	1.5	Zr	1.5	Yb	0.5			P	3			O	12	1.5	0.405	1.30×10^{-621}	
Na	1.8	Zr	1.2	Yb	0.8			P	3			O	12	1.8	0.414	4.02×10^{-621}	
Na	2	Zr	1	Yb	1			P	3			O	12	2	0.420	6.47×10^{-621}	
Na	2.2	Zr	0.8	Yb	1.2			P	3			O	12	2.2	0.426	5.23×10^{-621}	
Na	2.3	Zr	0.7	Yb	1.3			P	3			O	12	2.3	0.428	6.77×10^{-621}	
Na	2.5	Zr	0.5	Yb	1.5			P	3			O	12	2.5	0.434	2.91×10^{-621}	
Na	2.6	Zr	0.4	Yb	1.6			P	3			O	12	2.6	0.437	6.43×10^{-721}	
Na	2.8	Zr	0.2	Yb	1.8			P	3			O	12	2.8	0.443	3.17×10^{-721}	
Na	2.9	Zr	0.1	Yb	1.9			P	3			O	12	2.9	0.446	2.57×10^{-821}	
Na	1.5	Zr	1.5	Cr	0.5			P	3			O	12	1.5	0.380	4.81×10^{-721}	
Na	2	Zr	1	Cr	1			P	3			O	12	2	0.369	2.07×10^{-621}	
Na	2.3	Zr	0.7	Cr	1.3			P	3			O	12	2.3	0.363	5.91×10^{-621}	
Na	2.5	Zr	0.5	Cr	1.5			P	3			O	12	2.5	0.359	9.92×10^{-621}	
Na	2.7	Zr	0.3	Cr	1.7			P	3			O	12	2.7	0.354	6.04×10^{-621}	
Na	2.95	Zr	0.05	Cr	1.95			P	3			O	12	2.95	0.349	2.40×10^{-621}	
Na	3	Cr	2					P	3			O	12	3	0.348	3.63×10^{-921}	
Na	3	Zr	2				Si	2	P	0.6	As	0.4	O	12	3	0.439	6.66×10^{-422}
Na	3	Zr	1.6	Ti	0.4			P	1			O	12	3	0.521	4.12×10^{-422}	
Na	3	Zr	2	Ge	0.8		Si	1.2	P	0.6	As	0.4	O	12	3	0.482	6.44×10^{-422}
Na	3	Zr	1.6	Th	0.4		Si	2	P	1			O	12	3	0.444	9.21×10^{-422}
Na	3	Fe	2					P	3			O	12	3	0.360	1.17×10^{-823}	
Na	3	Cr	2					P	3			O	12	3	0.348	1.76×10^{-823}	
Na	1	Zr	2							As	3	O	12	1	0.489	4.11×10^{-724}	
Na	1.15	Zr	0.85	Yb	0.15				As	3	O	12	1.15	0.437	7.85×10^{-724}		
Na	1.25	Zr	0.75	Yb	0.25				As	3	O	12	1.25	0.441	1.10×10^{-624}		
Na	1.35	Zr	0.65	Yb	0.35				As	3	O	12	1.35	0.444	1.44×10^{-624}		
Na	1.55	Zr	0.55	Yb	0.45				As	3	O	12	1.55	0.448	1.83×10^{-624}		
Na	3	Zr	0.5	Sc	1.5		Si	0.5	P	1.5			O	12	3	0.466	7.42×10^{-525}

Na	2.7	Zr	1.8	Sc	0.2		Si	1.5	P	1.5		O	12	2.7	0.418	$2.46 \times 10^{-4.25}$
Na	3	Zr	1.8	Sc	0.2		Si	1.8	P	1.2		O	12	3	0.423	$3.40 \times 10^{-4.25}$
Na	1	Zr	2					P	3			O	12	1	0.390	$3.98 \times 10^{-9.26}$
Na	1.3	Zr	1.85	Mg	0.15			P	3			O	12	1.3	0.390	$1.03 \times 10^{-8.26}$
Na	1.6	Zr	1.7	Mg	0.3			P	3			O	12	1.6	0.390	$2.23 \times 10^{-8.26}$
Na	1.8	Zr	1.6	Mg	0.4			P	3			O	12	1.8	0.390	$2.28 \times 10^{-7.26}$
Na	2	Zr	1.5	Mg	0.5			P	3			O	12	2	0.390	$3.72 \times 10^{-7.26}$
Na	2.5	Zr	1.25	Mg	0.75			P	3			O	12	2.5	0.390	$7.94 \times 10^{-7.26}$
Na	3	Zr	1	Mg	1			P	3			O	12	3	0.390	$1.21 \times 10^{-6.26}$
Na	3.2	Zr	2	Si	2.2			P	0.8			O	12	3.2	0.430	$5.01 \times 10^{-4.27}$
Na	3.28	Zr	1.96	Mg	0.04		Si	2.2	P	0.8		O	12	3.28	0.430	$5.01 \times 10^{-4.27}$
Na	3.36	Zr	1.92	Mg	0.08		Si	2.2	P	0.8		O	12	3.36	0.430	$5.01 \times 10^{-4.27}$
Na	3.52	Zr	1.84	Mg	0.16		Si	2.2	P	0.8		O	12	3.52	0.430	$2.58 \times 10^{-4.27}$
Na	3.84	Zr	1.68	Mg	0.32		Si	2.2	P	0.8		O	12	3.84	0.430	$5.06 \times 10^{-6.27}$
Na	1	Zr	2					P	3			O	12	1	0.390	$1.71 \times 10^{-8.28}$
Na	1.5	Zr	1.5	Al	0.5			P	3			O	12	1.5	0.372	$4.31 \times 10^{-8.28}$
Na	1.5	Zr	1.5	Cr	0.5			P	3			O	12	1.5	0.380	$2.17 \times 10^{-7.28}$
Na	1.5	Zr	1.5	Ga	0.5			P	3			O	12	1.5	0.380	$3.02 \times 10^{-8.28}$
Na	1.5	Zr	1.5	In	0.5			P	3			O	12	1.5	0.398	$3.93 \times 10^{-7.28}$
Na	1.5	Zr	1.5	Sc	0.5			P	3			O	12	1.5	0.393	$1.30 \times 10^{-6.28}$
Na	1.5	Zr	1.5	Y	0.5			P	3			O	12	1.5	0.408	$1.99 \times 10^{-6.28}$
Na	1.5	Zr	1.5	Yb	0.5			P	3			O	12	1.5	0.405	$6.67 \times 10^{-7.28}$
Na	2	Zr	1	Al	1			P	3			O	12	2	0.353	$5.57 \times 10^{-9.28}$
Na	2	Zr	1	Cr	1			P	3			O	12	2	0.369	$6.54 \times 10^{-7.28}$
Na	2	Zr	1	Ga	1			P	3			O	12	2	0.370	$2.85 \times 10^{-9.28}$
Na	2	Zr	1	In	1			P	3			O	12	2	0.406	$3.16 \times 10^{-6.28}$
Na	2	Zr	1	Sc	1			P	3			O	12	2	0.395	$5.35 \times 10^{-6.28}$
Na	2	Zr	1	Y	1			P	3			O	12	2	0.426	$2.30 \times 10^{-7.28}$
Na	2	Zr	1	Yb	1			P	3			O	12	2	0.420	$3.98 \times 10^{-6.28}$
Na	2.5	Zr	0.5	Cr	1.5			P	3			O	12	2.5	0.359	$4.00 \times 10^{-6.28}$
Na	2.5	Zr	0.5	In	1.5			P	3			O	12	2.5	0.414	$1.39 \times 10^{-6.28}$
Na	2.5	Zr	0.5	Sc	1.5			P	3			O	12	2.5	0.398	$2.32 \times 10^{-5.28}$
Na	2.5	Zr	0.5	Y	1.5			P	3			O	12	2.5	0.444	$7.52 \times 10^{-7.28}$
Na	2.5	Zr	0.5	Yb	1.5			P	3			O	12	2.5	0.434	$3.11 \times 10^{-6.28}$
Na	3	In	2					P	3			O	12	3	0.422	$1.42 \times 10^{-7.28}$
Na	3	Cr	2					P	3			O	12	3	0.348	$2.43 \times 10^{-8.28}$

Na	3	Fe	2		P	3	O	12	3	0.360	$1.03 \times 10^{-7.28}$	
Na	3	Sc	2		P	3	O	12	3	0.400	$5.16 \times 10^{-5.28}$	
Na	1	Ge	2		P	3	O	12	1	0.314	$1.54 \times 10^{-15.29}$	
Na	1	Ge	1.5	Ti	0.5	P	3	O	12	1	$0.322 \times 10^{-13.29}$	
Na	1	Ge	1	Ti	1	P	3	O	12	1	$1.05 \times 10^{-11.29}$	
Na	1	Ge	0.5	Ti	1.5	P	3	O	12	1	$0.329 \times 10^{-10.29}$	
Na	1	Ti	2		P	3	O	12	1	0.344	$5.29 \times 10^{-9.29}$	
Na	1	Sn	2		P	3	O	12	1	0.378	$2.81 \times 10^{-11.29}$	
Na	1	Sn	1.5	Ti	0.5	P	3	O	12	1	$0.370 \times 10^{-11.29}$	
Na	1	Sn	1	Ti	1	P	3	O	12	1	$9.39 \times 10^{-11.29}$	
Na	1	Sn	0.5	Ti	1.5	P	3	O	12	1	$0.353 \times 10^{-10.29}$	
Na	1	Sn	2		P	3	O	12	1	0.378	$2.81 \times 10^{-11.29}$	
Na	1	Zr	0.5	Sn	1.5	P	3	O	12	1	$0.381 \times 10^{-11.29}$	
Na	1	Zr	1	Sn	1	P	3	O	12	1	$2.93 \times 10^{-10.29}$	
Na	1	Zr	1.5	Sn	0.5	P	3	O	12	1	$1.15 \times 10^{-9.29}$	
Na	1	Zr	2		P	3	O	12	1	0.390	$1.71 \times 10^{-8.29}$	
Na	2	Hf	2		P	3	O	12	2	0.386	$4.72 \times 10^{-9.29}$	
Na	1.5	Zr	1.5	Ga	0.5	P	3	O	12	1.5	0.380	$4.03 \times 10^{-8.30}$
Na	1.5	Zr	1.5	Cr	0.5	P	3	O	12	1.5	0.380	$5.33 \times 10^{-7.30}$
Na	1	Ti	2		P	3	O	12	1	0.344	$2.51 \times 10^{-14.31}$	
Na	1	Zr	2		P	3	O	12	1	0.390	$1.06 \times 10^{-8.31}$	
Na	1	Zr	1	Nb	1	P	3	O	12	1	0.374	$1.06 \times 10^{-8.31}$
Na	1	Ti	1	Nb	1	P	3	O	12	1	0.351	$1.25 \times 10^{-6.31}$
Na	1	Sc	1	Nb	1	P	3	O	12	1	0.379	$1.16 \times 10^{-11.32}$
Na	1.5	Sc	1	Nb	1	P	3	O	12	1.5	0.379	$5.42 \times 10^{-7.32}$
Na	2	Sc	1	Nb	1	P	3	O	12	2	0.379	$8.39 \times 10^{-7.32}$
Na	2.5	Sc	1	Nb	1	P	3	O	12	2.5	0.379	$1.62 \times 10^{-6.32}$
Na	3	Sc	1	Nb	1	P	3	O	12	3	0.379	$2.13 \times 10^{-6.32}$
Na	1	Zr	2		P	3	O	12	1	0.390	$4.46 \times 10^{-9.33}$	
Na	1.4	Zr	1.6	In	0.4	P	3	O	12	1.4	0.396	$1.43 \times 10^{-7.33}$
Na	1.6	Zr	1.4	In	0.6	P	3	O	12	1.6	0.400	$6.17 \times 10^{-7.33}$
Na	1.8	Zr	1.2	In	0.8	P	3	O	12	1.8	0.403	$8.86 \times 10^{-7.33}$
Na	2	Zr	1	In	1	P	3	O	12	2	0.406	$2.20 \times 10^{-6.33}$
Na	2.2	Zr	0.8	In	1.2	P	3	O	12	2.2	0.409	$2.48 \times 10^{-6.33}$
Na	2.4	Zr	0.6	In	1.4	P	3	O	12	2.4	0.412	$3.77 \times 10^{-6.33}$
Na	1.2	Zr	1.8	Yb	0.2	P	3	O	12	1.2	0.396	$1.56 \times 10^{-7.33}$

Na	1.4	Zr	1.6	Yb	0.4	P	3	O	12	1.4	0.402	$2.19 \times 10^{-7\,33}$
Na	1.6	Zr	1.4	Yb	0.6	P	3	O	12	1.6	0.408	$7.59 \times 10^{-7\,33}$
Na	1.8	Zr	1.2	Yb	0.8	P	3	O	12	1.8	0.414	$2.68 \times 10^{-6\,33}$
Na	2	Zr	1	Yb	1	P	3	O	12	2	0.420	$1.83 \times 10^{-6\,33}$
Na	2.4	Zr	0.6	Yb	1.4	P	3	O	12	2.4	0.431	$1.95 \times 10^{-6\,33}$
Na	2.6	Zr	0.4	Yb	1.6	P	3	O	12	2.6	0.437	$1.56 \times 10^{-6\,33}$
Na	2.8	Zr	0.2	Yb	1.8	P	3	O	12	2.8	0.443	$3.66 \times 10^{-8\,33}$
Na	1.4	Al	0.4	Ti	1.6	P	3	O	12	1.4	0.338	$1.06 \times 10^{-7\,34}$
Na	1.4	Al	0.4	Sn	1.6	P	3	O	12	1.4	0.366	$1.24 \times 10^{-8\,34}$
Na	1.4	Al	0.4	Ge	1.6	P	3	O	12	1.4	0.314	$6.64 \times 10^{-10\,34}$

References

1. Shannon, R. D. Revised effective ionic radii and systematic studies of interatomic distances in halides and chalcogenides. *Acta Crystallogr.* **1976**, *A32*, 751-767. DOI: 10.1107/S0567739476001551
2. Willems, T. F.; Rycroft, C. H.; Kazi, M.; Meza, J. C.; Haranczyk, M. Algorithms and tools for high-throughput geometry-based analysis of crystalline porous materials. *Microporous Mesoporous Mater.* **2012**, *149* (1), 134-141. DOI: 10.1016/j.micromeso.2011.08.020
3. Ongari, D.; Boyd, P. G.; Barthel, S.; Witman, M.; Haranczyk, M.; Smit, B. Accurate characterization of the pore volume in microporous crystalline materials. *Langmuir* **2017**, *33* (51), 14529-14538. DOI: 10.1021/acs.langmuir.7b01682
4. Kieschnick, R.; McCullough, B. D. Regression analysis of variates observed on (0, 1): percentages, proportions and fractions. *Stat. Modelling* **2003**, *3* (3), 193-213. DOI: 10.1191/1471082X03st053oa
5. Ferrari, S.; Cribari-Neto, F. Beta regression for modelling rates and proportions. *J. Appl. Stat.* **2004**, *31* (7), 799-815. DOI: 10.1080/0266476042000214501
6. Jang, S.-H.; Tateyama, Y.; Jalem, R. High-throughput data-driven prediction of stable high-performance Na-ion sulfide solid electrolytes. *Adv. Funct. Mater.* **2022**, *32* (48), 2206036. DOI: 10.1002/adfm.202206036

7. Heyd, J.; Peralta, J. E.; Scuseria, G. E.; Martin, R. L. Energy band gaps and lattice parameters evaluated with the Heyd-Scuseria-Ernzerhof screened hybrid functional. *J. Chem. Phys.* **2005**, *123*, 174101. DOI: 10.1063/1.2085170
8. Klimeš, J.; Bowler, D. R.; Michaelides, A. Van der Waals density functionals applied to solids. *Phys. Rev. B* **2011**, *83*, 195131. DOI: 10.1103/PhysRevB.83.195131
9. Fujitsu, S.; Nagai, M.; Kanazawa, T.; Yasui, I. Conduction paths in sintered ionic conductive material $\text{Na}_{1+x}\text{Y}_x\text{Zr}_{2-x}(\text{PO}_4)_3$. *Mater. Res. Bull.* **1981**, *16* (10), 1299-1309. DOI: 10.1016/0025-5408(81)90101-X
10. Perthuis, H.; Colomban, Ph. Well densified NASICON type ceramics, elaborated using sol-gel process and sintering at low temperatures. *Mater. Res. Bull.* **1984**, *19* (5), 621-631. DOI: 10.1016/0025-5408(84)90130-2
11. Vogel, E. M.; Cava, R. J.; Rietman, E. Na^+ ion conductivity and crystallographic cell characterization in the Hf-nasicon system $\text{Na}_{1+x}\text{Hf}_2\text{Si}_x\text{P}_{3-x}\text{O}_{12}$. *Solid State Ion.* **1984**, *14* (1), 1-6. DOI: 10.1016/0167-2738(84)90002-X
12. Fuentes, R. O.; Figueiredo, F. M.; Soares, M. R.; Marques, F. M. B. Submicrometric NASICON ceramics with improved electrical conductivity obtained from mechanically activated precursors. *J. Eur. Ceram. Soc.* **2005**, *25* (4), 455-462. DOI: 10.1016/j.jeurceramsoc.2004.02.019
13. Guin, M.; Tietz, F.; Guillot, O. New promising NASICON material as solid electrolyte for sodium-ion batteries: Correlation between composition, crystal structure and ionic conductivity of $\text{Na}_{3+x}\text{Sc}_2\text{Si}_x\text{P}_{3-x}\text{O}_{12}$. *Solid State Ion.* **2016**, *293* (1), 18-26. DOI: 10.1016/j.ssi.2016.06.005

14. Song, S.; Duong, H. M.; Korsunsky, A. M.; Hu, N.; Lu, L. A Na^+ superionic conductor for room-temperature sodium batteries. *Sci. Rep.* **2016**, *6*, 32330. DOI: 10.1038/srep32330
15. Khakpour, Z. Influence of M : Ce^{4+} , Gd^{3+} and Yb^{3+} substituted $\text{Na}_{3+x}\text{Zr}_{2-x}M_x\text{Si}_2\text{PO}_{12}$ solid NASICON electrolytes on sintering, microstructure and conductivity. *Electrochim. Acta*. **2016**, *196*, 337-347. DOI: 10.1016/j.electacta.2016.02.199
16. Ma, Q.; Guin, M.; Naqash, S.; Tsai, C.-L.; Tietz, F.; Guillon, O. Scandium-substituted $\text{Na}_3\text{Zr}_2(\text{SiO}_4)_2(\text{PO}_4)$ prepared by a solution-assisted solid-state reaction method as sodium-ion conductors. *Chem. Mater.* **2016**, *28* (13), 4821-4828. DOI: 10.1021/acs.chemmater.6b02059
17. Lu, Y.; Alonso, J. A.; Yi, Q.; Lu, L.; Wang, Z. L.; Sun, C. A high-performance monolithic solid-state sodium battery with Ca^{2+} doped $\text{Na}_3\text{Zr}_2\text{Si}_2\text{PO}_{12}$ electrolyte. *Adv. Energy Matter.* **2019**, *9* (28), 1901205. DOI: 10.1002/aenm.201901205
18. Liu, Y.; Liu, L.; Peng, J.; Zhou, X.; Liang, D.; Zhao, L.; Su, J.; Zhang, B.; Li, S.; Zhang, N.; Ma, Q.; Tietz, F. A niobium-substituted sodium superionic conductor with conductivity higher than 5.5 mScm^{-1} prepared by solution-assisted solid-state reaction method. *J. Power Sources*, **2022**, *518*, 230765. DOI: 10.1016/j.jpowsour.2021.2307654
19. Stainer, F.; Gadermaier, B.; Kügerl, A.; Ladenstein, L.; Hogrefe, K.; Wilkening, H. M. R. Fast Na^+ Ion Dynamics in the Nb^{5+} Bearing NaSICON $\text{Na}_{3+x-z}\text{Nb}_z\text{Zr}_{2-z}\text{Si}_{2+x}\text{P}_{1-x}\text{O}_{12}$ as Probed by ^{23}Na NMR and Conductivity Spectroscopy. *Solid State Ion.* **2023**, *395*, 116209. DOI: 10.1016/j.ssi.2023.116209.

20. Takahashi, T.; Kuwabara, K.; Shibata, M. Solid-state ionics - conductivities of Na^+ ion conductors based on NASICON. *Solid State Ion.* **1980**, *1* (3-4), 163-175. DOI: 10.1016/0167-2738(80)90001-6
21. Delmas, C.; Viala, J.-C.; Olazcuaga, R.; Le Flem, G.; Hagenmuller, P.; Cherkaoui, F.; Brochu, R. Ionic conductivity in Nasicon-type phases $\text{Na}_{1+x}\text{Zr}_{2-x}L_x(\text{PO}_4)_3$ ($L = \text{Cr, In, Yb}$). *Solid State Ion.* **1981**, *3-4*, 209-214. DOI: 10.1016/0167-2738(81)90084-9
22. Cava, R. J.; Vogel, E. M.; Johnson Jr., D. W. Effect of homovalent framework cation substitutions on the sodium ion conductivity in $\text{Na}_3\text{Zr}_2\text{Si}_2\text{PO}_{12}$. *J. Am. Ceram. Soc.* **1982**, *65* (9), c157-c159. DOI: 10.1111/j.1151-2916.1982.tb10526.x
23. d'Yvoire, F.; Pintard-Scrépel, M.; Bretey, E.; de la Rochère, M. Phase transitions and ionic conduction in 3D skeleton phosphates $A_3M_2(\text{PO}_4)_3$: $A = \text{Li, Na, Ag, K}$; $M = \text{Cr, Fe}$. *Solid State Ion.* **1983**, *9-10* (2), 851-857. DOI: 10.1016/0167-2738(83)90101-7
24. Zahir, M.; Olazcuaga, R.; Hagenmuller, P. Crystal chemistry and ionic conductivity in Nasicon-type phases $\text{Na}_{1+x}\text{Zr}_{2-x}\text{Yb}_x(\text{AsO}_4)_3$ with $0 \leq x \leq 0.45$. *Mater. Lett.* **1984**, *2* (3), 234-236. DOI: 10.1016/0167-577X(84)90032-6
25. Subramanian, M. A.; Rudolf, P. R.; Clearfield, A. The preparation, structure, and conductivity of scandium-substituted NASICONs. *J. Solid State Chem.* **1985**, *60* (2), 172-181. DOI: 10.1016/0022-4596(85)90109-4
26. Cherkaoui, F.; Viala, J. C.; Delmas, C.; Hagenmuller, P. Crystal chemistry and ionic conductivity of a new Nasicon-related solid solution $\text{Na}_{1+x}\text{Zr}_{2-x}\text{Mg}_{x2}(\text{PO}_4)_3$. *Solid State Ion.* **1986**, *21* (4), 333-337. DOI: 10.1016/0167-2738(86)90195-5

27. Krok, F.; Kony, D.; Dygas, J. R.; Jakubowski, W.; Bogusz, W. On some properties of NASICON doped with MgO and CoO. *Solid State Ion.* **1989**, *36* (3-4), 251-254. DOI: 10.1016/0167-2738(89)90184-7
28. Winand, J. M.; Rulmont, A.; Tarte, P. Ionic conductivity of the $\text{Na}_{1+x}M^{\text{III}}_x\text{Zr}_{2-x}(\text{PO}_4)_3$ systems ($M = \text{Al, Ga, Cr, Fe, Sc, In, Y, Yb}$). *J. Mater. Sci.* **1990**, *25*, 4008-4013. DOI: 10.1007/BF00582473
29. Winand, J. M.; Rulmont, A.; Tarte, P. Nouvelles solutions solides $L^{\text{I}}(M^{\text{IV}})_{2-x}(N^{\text{IV}})_x(\text{PO}_4)_3$ ($L = \text{Li, Na}$ $M, N = \text{Ge, Sn, Ti, Zr, Hf}$) synthèse et étude par diffraction x et conductivité ionique. *J. Solid State Chem.* **1991**, *93* (2), 341-349. DOI: 10.1016/0022-4596(91)90308-5
30. Saito, Y.; Ado, K.; Asai, T.; Kageyama, H.; Nakamura, O. Ionic conductivity of NASICON-type conductors $\text{Na}_{1.5}M_{0.5}\text{Zr}_{1.5}(\text{PO}_4)_3$ ($M: \text{Al}^{3+}, \text{Ga}^{3+}, \text{Cr}^{3+}, \text{Sc}^{3+}, \text{Fe}^{3+}, \text{In}^{3+}, \text{Yb}^{3+}, \text{Y}^{3+}$). *Solid State Ion.* **1992**, *58* (3-4), 327-331. DOI: 10.1016/0167-2738(92)90136-D
31. Bennouna, L.; Arsalane, S.; Brochu, R.; Lee, M. R.; Chassaing, J.; Quarton, M. Spécificités des ions Nb^{IV} et Mo^{IV} dans les monophosphates de type Nasicon. *J. Solid State Chem.* **1995**, *114* (1), 224-229. DOI: 10.1006/jssc.1995.1032
32. Znaidi, L.; Launay, S.; Quarton, M. Crystal chemistry and electrical properties of $\text{Na}_{1+x}\text{ScNb}(\text{PO}_4)_3$ phases. *Solid State Ion.* **1997**, *93* (3-4), 273-277. DOI: 10.1016/S0167-2738(96)00558-9
33. Miyajima, Y.; Miyoshi, T.; Tamaki, J.; Matsuoka, M.; Yamamoto, Y.; Masquelier, C.; Tabuchi, M.; Saito, Y.; Kageyama, H. Solubility range and ionic conductivity of large trivalent

ion doped $\text{Na}_{1+x}M_x\text{Zr}_{2-x}\text{P}_3\text{O}_{12}$ (M : In, Yb, Er, Y, Dy, Tb, Gd) solid electrolytes. *Solid State Ion.* **1999**, *124* (3-4), 201-211. DOI: 10.1016/S0167-2738(99)00116-2

34. Maldonado-Manso, P.; Aranda, M. A. G.; Bruque, S.; Sanz, J.; Losilla, E. R. Nominal vs. actual stoichiometries in Al-doped NASICONs: A study of the $\text{Na}_{1.4}\text{Al}_{0.4}M_{1.6}(\text{PO}_4)_3$ (M = Ge, Sn, Ti, Hf, Zr) family. *Solid State Ion.* **2005**, *176* (17-18), 1613-1625. DOI: 10.1016/j.ssi.2005.04.009